Measurements of the budgets of the subgrid-scale stress and temperature flux in a convective atmospheric surface layer

Khuong X. Nguyen[1], **Thomas W. Horst**[2], **Steven P. Oncley**[2]
and Chenning Tong[1],†

[1]Department of Mechanical Engineering, Clemson University, Clemson, SC 29634, USA
[2]National Center for Atmospheric Research, Boulder, CO 80307, USA

The dynamics of the subgrid-scale (SGS) stress and scalar flux in the convective atmospheric surface layer are studied through the budgets of the SGS turbulence kinetic energy (TKE), the SGS stress and the SGS temperature flux using field measurements from the Advection Horizontal Array Turbulence Study (AHATS). The array technique, which employs sensor arrays to perform filter operations to obtain the SGS velocity and temperature, is extended to include pressure sensors to measure the fluctuating pressure, enabling separation of the resolvable- and subgrid-scale pressure, and therefore for the first time allowing for measurement of the pressure covariance terms and the full SGS budgets. The non-dimensional forms of the SGS budget terms are obtained as functions of the stability parameter z/L and the ratio of the wavelength of the spectral peak of the vertical velocity to the filter width, Λ_w/Δ_f. The results show that the SGS TKE budget is a balance among the production, transport and dissipation. The SGS shear stress budget and the SGS temperature flux budgets are dominated by the production and pressure destruction, with the latter causing return to isotropy. The budgets of the SGS normal stress components are more complex. Most notably the pressure–strain-rate correlation includes two competing processes, return to isotropy and generation of anisotropy, the latter due to ground blockage of the large convective eddies. For neutral surface layers, return to isotropy dominates. For unstable surface layers return to isotropy dominates for small filter widths, whereas for large filter widths the ground blockage effect dominates, resulting in strong anisotropy. The results in the present study, particularly for the pressure–strain-rate correlation, have strong implications for modelling the SGS stress and flux using their transport equations in the convective atmospheric boundary layer.

Key words: atmospheric flows, turbulence modelling, turbulent boundary layers

1. Introduction

Large-eddy simulation (LES) has become an important approach for simulating turbulent flows. LES computes the large, or resolvable, scales of the flow field and

† Email address for correspondence: ctong@ces.clemson.edu

models the effects of the smaller, or subgrid, scales. The premise of LES is that if the filter scale is in the inertial range, the energy-containing scales are well-resolved and most of the turbulent stress and flux are carried by the resolvable scales (Lilly 1967; Domaradzki, Liu & Brachet 1993; Borue & Orszag 1998); therefore, the statistics of the energy-containing scales obtained by LES are insensitive to the subgrid-scale (SGS) model employed as long as it provides the correct energy transfer rate from the resolvable scales (Lilly 1967; Nieuwstadt & de Valk 1987; Domaradzki *et al.* 1993; Mason 1994; Borue & Orszag 1998; Wyngaard 2004). This is indeed the case for some lower-order statistics, such as the mean and root mean square (r.m.s.) profiles in the atmospheric mixed layer (e.g. Nieuwstadt *et al.* 1991; Mason 1994; Mason & Brown 1994). In LES of high-Reynolds-number turbulent boundary layers, however, the filter scale in the near-wall region is inevitably in the energy-containing scale range (Kaimal *et al.* 1972; Mason 1994; Peltier *et al.* 1996; Tong *et al.* 1998; Tong, Wyngaard & Brasseur 1999), leading to inherent under-resolution of the LES field. As a result, significant portions of the turbulent stress and flux in the region are carried by the SGS model, resulting in strong dependence of near-wall results on the model employed (e.g. Mason & Thomson 1992; Tong *et al.* 1999). Consequently, deficiencies in the SGS model are likely to lead to inaccuracies in near-wall LES statistics. It has also been observed in LES that the errors in the surface layer can propagate into the mixed layer and alter the flow structure there (e.g. Khanna & Brasseur 1998; Ludwig, Chow & Street 2009).

The majority of the current SGS models are based on direct modelling of the SGS stress (first-order models) using the resolvable-scale strain-rate tensor or the resolvable-scale velocity gradient tensor, such as the Smagorinsky model (Smagorinsky 1963; Lilly 1967; Deardorff 1970) and its variants (e.g. Schumann 1975; Deardorff 1980; Métais & Lesieur 1992), similarity models (Bardina, Ferziger & Reynolds 1980), nonlinear models (Leonard 1974; Clark, Ferziger & Reynolds 1979; Vreman, Geurts & Kuerten 1994), and the dynamic model (Germano *et al.* 1991) and its variants (Meneveau, Lund & Cabot 1996; Porté-Agel *et al.* 2000). The advantages of these models are their relative functional simplicity and low computational cost compared to more complex models (e.g. transport equation-based models). The physics that can be incorporated into these models, however, is very limited (Wyngaard 2004; Hatlee & Wyngaard 2007).

At the next level, transport equations can be used to model the SGS stress and flux. In this class of models, the transport equations for the full SGS stress tensor are solved, allowing for more physics (including history and non-local effects) to be incorporated into the model (Deardorff 1972, 1973; Wyngaard 2004; Hatlee & Wyngaard 2007). Previous transport equation models are largely based on Reynolds stress models. A review of the models for the terms in the Reynolds stress transport equation is given by Lumley (1983). Here, the production term is in closed form and dissipation is assumed to be isotropic. Turbulent transport is modelled using gradient diffusion or a transport equation, particularly for unstable surface layers. The pressure term is decomposed into a transport term and a pressure–strain-rate correlation. The former is often modelled along with turbulent transport. The latter is further decomposed into a 'slow' and a 'rapid' part. The slow part is modelled as a return-to-isotropy term (Rotta 1951), similar to that for neutral atmospheric boundary layers (ABLs) and other flows without buoyancy effects. A number of models exist for the rapid term (e.g. Launder, Reece & Rodi 1975; Shih & Lumley 1985; Fu, Launder & Tselepidakis 1987). An important aspect of these models is that they take into

account the effects of the transport properties of the surface layer turbulence on the Reynolds stress.

While the dynamics of the Reynolds stress and scalar flux depend on the stability condition of the ABL, the dynamics of the SGS stress and flux also depend on the filter scale, and can have characteristics significantly different from those of the Reynolds stress and flux. Developing transport equation-based SGS models, therefore, requires knowledge of the dynamics of the SGS stress and scalar flux. In the present study we investigate the SGS dynamics in near-neutral and unstable atmospheric surface layers. The budgets of the SGS turbulence kinetic energy (TKE), the SGS stress and the SGS temperature flux are obtained from field measurements and examined to gain insights into the SGS dynamics.

The transport equation for the SGS stress deduced from the Navier–Stokes equations is (e.g. Lilly 1967)

$$\frac{\partial \tau_{ij}}{\partial t} + u_k^r \frac{\partial \tau_{ij}}{\partial x_k} = \frac{\partial}{\partial x_k} T_{ijk}^{(t)} + P_{ij} + P_{Bij} + \Pi_{ij} - \epsilon_{sij} - \nu \frac{\partial \tau_{ij}}{\partial x_k \partial x_k}, \tag{1.1}$$

where $\tau_{ij} = (u_i u_j)^r - u_i^r u_j^r$ is the (kinematic) SGS stress. A superscript r denotes a resolvable-scale variable. The terms on the left-hand side of (1.1) represent the time the rate of change and advection of τ_{ij}, respectively. The terms on the right-hand side are the turbulent transport of τ_{ij}

$$\frac{\partial}{\partial x_k} T_{ijk}^{(t)} = \frac{\partial}{\partial x_k} [u_k^r (u_i u_j)^r - (u_i u_j u_k)^r + (\tau_{ik} u_j^r + \tau_{jk} u_i^r)], \tag{1.2}$$

the rate of mechanical production

$$P_{ij} = - \left(\tau_{ik} \frac{\partial u_j^r}{\partial x_k} + \tau_{jk} \frac{\partial u_i^r}{\partial x_k} \right), \tag{1.3}$$

the rate of buoyant production

$$P_{Bij} = \frac{g}{\Theta} \{ \delta_{i3} [(\theta u_j)^r - \theta^r u_j^r] + \delta_{j3} [(\theta u_i)^r - \theta^r u_i^r] \}, \tag{1.4}$$

the velocity–pressure-gradient correlation

$$\Pi_{ij} = - \left[\left(u_i \frac{\partial p}{\partial x_j} + u_j \frac{\partial p}{\partial x_i} \right)^r - \left(u_i^r \frac{\partial p^r}{\partial x_j} + u_j^r \frac{\partial p^r}{\partial x_i} \right) \right], \tag{1.5}$$

the rate of viscous dissipation

$$\epsilon_{sij} = 2\nu \left[\left(\frac{\partial u_i}{\partial x_k} \frac{\partial u_j}{\partial x_k} \right)^r - \frac{\partial u_i^r}{\partial x_k} \frac{\partial u_j^r}{\partial x_k} \right], \tag{1.6}$$

and the rate of viscous transport, respectively. Here, u_i, p, Θ, θ, g and ν are the velocity, kinematic pressure, mean and fluctuating potential temperatures, gravitational acceleration and kinematic viscosity, respectively. The SGS velocity–pressure-gradient correlation can be decomposed into a pressure–strain-rate correlation and a pressure transport term,

$$\Pi_{ij} = \mathscr{R}_{ij} - \frac{\partial}{\partial x_k} T_{ijk}^{(p)}, \tag{1.7}$$

respectively, where

$$\mathcal{R}_{ij} = \left(p\frac{\partial u_i}{\partial x_j} + p\frac{\partial u_j}{\partial x_i} \right)^r - \left(p^r\frac{\partial u_i^r}{\partial x_j} + p^r\frac{\partial u_j^r}{\partial x_i} \right) \tag{1.8}$$

is the SGS pressure–strain-rate correlation tensor and

$$T_{ijk}^{(p)} = \delta_{jk}[(pu_i)^r - p^r u_i^r] + \delta_{ik}[(pu_j)^r - p^r u_j^r]. \tag{1.9}$$

Contracting (1.1) yields the transport equation for the SGS TKE,

$$\frac{\partial k}{\partial t} + u_k^r\frac{\partial k}{\partial x_k} = \frac{1}{2}\frac{\partial}{\partial x_k}T_{iik}^{(t)} + \mathcal{P} + \mathcal{P}_B + \frac{1}{2}\frac{\partial}{\partial x_k}T_{iik}^{(p)} - \epsilon_{ks} - \nu\frac{\partial k}{\partial x_k \partial x_k}, \tag{1.10}$$

where $k = [(u_i u_i)^r - u_i^r u_i^r]/2$ is the SGS TKE. The terms on the left-hand side of (1.10) are the time rate of change and advection of k, respectively. The terms on the right-hand side are the turbulent transport of k

$$\frac{1}{2}\frac{\partial}{\partial x_k}T_{iik}^{(t)} = \frac{1}{2}\frac{\partial}{\partial x_k}\left[u_k^r(u_i u_i)^r - (u_i u_i u_k)^r + 2u_i^r(u_i u_k)^r - 2u_i^r u_i^r u_k^r \right], \tag{1.11}$$

the rate of mechanical production

$$\mathcal{P} = -\frac{1}{2}\tau_{ij}\left(\frac{\partial u_i^r}{\partial x_j} + \frac{\partial u_j^r}{\partial x_i} \right), \tag{1.12}$$

the rate of buoyant production

$$\mathcal{P}_B = \frac{g}{\Theta}[(\theta u_3)^r - \theta^r u_3^r], \tag{1.13}$$

the rate of pressure transport

$$\frac{1}{2}\frac{\partial}{\partial x_k}T_{iik}^{(p)} = -\frac{1}{2}\frac{\partial}{\partial x_k}[(2pu_k)^r - 2p^r u_k^r], \tag{1.14}$$

the rate of viscous dissipation

$$\epsilon_{ks} = \nu\left[\left(\frac{\partial u_i}{\partial x_k}\frac{\partial u_i}{\partial x_k} \right)^r - \frac{\partial u_i^r}{\partial x_k}\frac{\partial u_i^r}{\partial x_k} \right], \tag{1.15}$$

and the rate of viscous transport, respectively. Because the filter scale is much larger than the Kolmogorov scale in the surface layer (typically less than 1 mm), the viscous dissipation rate is almost entirely in the subgrid scales. Also note that the pressure–strain-rate correlation acts to redistribute energy among the three normal SGS stress components, and therefore sums to zero in (1.10).

The transport equation for the SGS temperature flux is

$$\frac{\partial F_i}{\partial t} + u_k^r\frac{\partial F_i}{\partial x_k} = \frac{\partial}{\partial x_k}T_{Fik}^{(t)} + P_{Fi} + P_{BFi} + \Pi_{Fi}, \tag{1.16}$$

where $F_i = (\theta u_i)^r - \theta^r u_i^r$ is the SGS temperature flux in the ith direction. The terms on the left-hand side of (1.16) are the time rate of change and advection of F_i, respectively. The terms on the right-hand side are, in order, the turbulent transport of F_i

$$\frac{\partial}{\partial x_k}T_{Fik}^{(t)} = -\frac{\partial}{\partial x_k}[(\theta u_i u_k)^r - \theta^r(u_i u_k)^r - u_i^r(\theta u_k)^r - u_k^r(\theta u_i)^r + 2\theta^r u_i^r u_k^r], \tag{1.17}$$

the rate of gradient (stratification) production and tilting production

$$P_{Fi} = -\tau_{ik}\frac{\partial \theta^r}{\partial x_k} - F_k\frac{\partial u_i^r}{\partial x_k}, \tag{1.18}$$

respectively, the rate of buoyant production

$$P_{BFi} = \delta_{i3}\frac{g}{\Theta}\left[(\theta^2)^r - (\theta^r)^2\right] \tag{1.19}$$

and the temperature–pressure-gradient correlation

$$\Pi_{Fi} = -\left[\left(\theta\frac{\partial p}{\partial x_i}\right)^r - \theta^r\frac{\partial p^r}{\partial x_i}\right]. \tag{1.20}$$

The SGS temperature–pressure-gradient correlation can be decomposed into a correlation between the fluctuating pressure and temperature-gradient and a transport term representing heat flux divergences due to the fluctuating pressure,

$$\Pi_{Fi} = \mathscr{R}_{Fi} - \frac{\partial}{\partial x_k}T_{Fik}^{(p)}, \tag{1.21}$$

respectively, where

$$\mathscr{R}_{Fi} = \left(p\frac{\partial \theta}{\partial x_i}\right)^r - p^r\frac{\partial \theta^r}{\partial x_i} \tag{1.22}$$

and

$$T_{Fik}^{(p)} = \delta_{ik}\left[(p\theta)^r - p^r\theta^r\right]. \tag{1.23}$$

The terms in the SGS transport equations contain important SGS mechanisms, thereby allowing for more physics to be incorporated into the models. Such SGS models have the potential to provide improved performance under a wide variety of flows and conditions, especially when first-order models might fail, in a way similar to the Reynolds stress models (Lumley 1983).

Our previous studies have shown that the dynamics of the SGS stress and temperature flux have a strong influence on the joint probability density function (j.p.d.f.) of the resolvable-scale velocity and temperature (Chen & Tong 2006; Chen, Liu & Tong 2010). Analyses of the SGS stress, the SGS stress production rate, the SGS temperature flux and the SGS temperature flux production rate conditional on the resolvable-scale velocity and temperature show that their statistics are closely related to the dynamics of the surface layer, particularly the strong buoyancy and vertical shear associated with updrafts and the conditional energy backscatter and isotropy of the SGS stress associated with downdrafts. Hence, buoyancy, shear and the ground blockage effect play an important role in the physics of the SGS stress and flux, suggesting that an ideal SGS model should incorporate surface-layer effects in order to correctly predict LES statistics. In the present study, we investigate the budgets of the SGS stress and scalar flux by examining the dependence of the unclosed SGS terms on the stability parameter and the filter width.

2. AHATS field campaign

The field measurements for this study, named the Advection Horizontal Array Turbulence Study (AHATS), were conducted in the San Joaquin Valley, California, during the summer of 2008 as a collaboration between Clemson University, Penn

Array spacing	Start PDT	End PDT	d_y (m)	d_x (m)	z_p (m)	z_s (m)	z_u (m)
Wide 1	12:00 25 June	12:00 01 July	4.00	16.00	3.24	4.24	3.74
Wide 2	13:00 01 July	06:00 18 July	4.00	16.00	3.24	4.24	3.24
Medium 1	16:00 20 July	06:00 29 July	1.29	5.12	3.64	4.64	3.64
Medium 2	12:30 29 July	06:00 08 August	1.29	5.12	4.83	5.83	4.83
Narrow	18:00 09 August	09:00 16 August	0.43	3.12	6.98	7.98	6.98

TABLE 1. AHATS array configurations. The streamwise array separation distance, d_x, was chosen to minimize flow distortion at the downwind array. However, as a precaution, the upwind arrays of the 'medium 2' and 'narrow' configurations were also staggered by $+17.23$ and $+5.74$ m in the y direction, respectively. Supplementary photographs of the arrays are available at http://dx.doi.org/10.1017/jfm.2013.302.

State University and the National Center for Atmospheric Research (NCAR). The field site is identical to that of the previous HATS field study (described by Horst *et al.* 2004) and is located 5.6 km east–northeast of Kettleman City, California, within an area of flat, fallow farmland. Sky conditions were predominantly clear, generally with persistent, predictable wind directions from the north to northwest. The field surface consisted of crop stubble and weeds, for which the displacement height and surface roughness (determined using near-neutral wind profiles from HATS) were approximately 32 and 2 cm, respectively. Homogeneous surface roughness continues at least 2 km in the upwind (northwest) direction and 1 km downwind. Field measurements for AHATS were obtained using the Integrated Surface Flux System (ISFS) and Integrated Sounding System (ISS), both deployed by NCAR, from 25 June to 16 August 2008. The ISFS consists of multiple sensors, deployed in an array, for detailed examination of the turbulence structure of the atmospheric surface layer through measurements of near-surface wind, temperature and pressure (discussed in detail below). The ISS was used to examine the heights beyond the surface layer using a wind profiler radar, sodar and radiosondes.

The field measurement design is based on the transverse array technique, proposed, studied and first implemented successfully by Tong *et al.* (1997, 1998, 1999) for surface-layer measurements in the ABL. In the context of LES, the technique uses horizontal sensor arrays to perform two-dimensional filtering to obtain resolvable- and subgrid-scale variables. It has subsequently been implemented in the ABL over land and ocean (Porté-Agel *et al.* 2001; Kleissl, Meneveau & Parlange 2003; Horst *et al.* 2004; Sullivan *et al.* 2006), within vegetation (Patton *et al.* 2011), over a glacier (Bou-Zeid *et al.* 2010) and in engineering flows (Cerutti, Meneveau & Knio 2000; Tong 2001; Wang & Tong 2002; Rajagopalan & Tong 2003; Chen *et al.* 2003; Wang, Tong & Pope 2004). Similar to these field studies, AHATS uses two vertically spaced arrays of sensors, shown in figure 1(*b*), to obtain filtered variables and their derivatives. The primary (lower) array consists of 13 equally spaced three-component sonic anemometer–thermometers (Campbell Scientific CSAT3), while the secondary (upper) array has nine. The arrays are centred in the lateral direction and aligned perpendicular to the prevailing wind direction.

In AHATS, a third line of nine sonic anemometers was added upwind to measure spatial differences in the streamwise direction (see figure 1*a* and table 1; the data are not used in the present study but will be examined in future analyses of the budgets
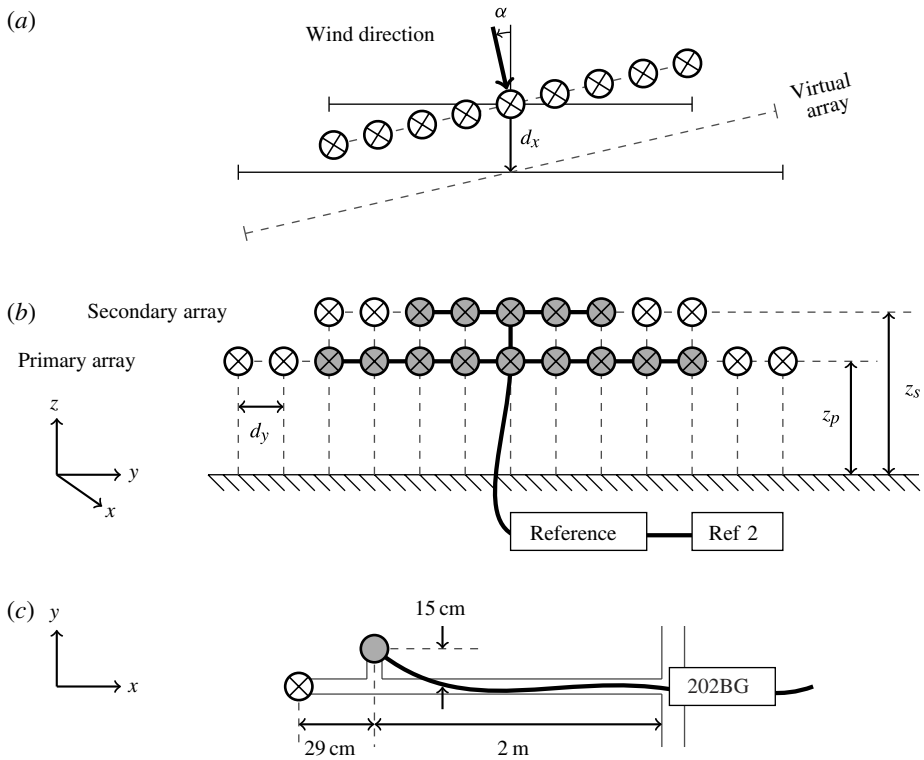
FIGURE 1. (*a*) Top view of arrays. The upwind and downwind arrays are centred laterally; z_u is the height of the upwind array and d_x the streamwise separation distance. Dashed lines denote virtual arrays aligned perpendicular to the mean wind direction. (*b*) Front view of downwind array. Sonic anemometers $\otimes$ in the primary and secondary arrays are located at heights z_p and z_s, respectively; the horizontal spacing is d_y. Pressure ports $\bigcirc$ are embedded at the centre of the sonic arrays. (*c*) Top view of an individual mast. The reference side of the pressure transducers are connected to a common reference reservoir through thin tubing ▬▬. An additional transducer measures the reference pressure using a second reference reservoir. Supplementary photographs of the arrays are available at http://dx.doi.org/10.1017/jfm.2013.302.

of the conditional SGS stress). In addition, two lines of turbulent pressure probes were added to measure, for the first time, the resolvable- and subgrid-scale pressure. The primary pressure array contains nine probes and is embedded at the centre of the lower (downwind) sonic anemometer array; the secondary pressure array contains five pressure probes embedded within the upper sonic anemometer array. The pressure probes are mounted level with the sonic anemometers, and are offset by approximately $+29$ and $+15$ cm in the x and y directions (as defined in figure 1*c*), respectively, relative to the sonic anemometers to avoid interference with velocity measurements (e.g. flow-induced distortion (Wyngaard 1981; Miller, Tong & Wyngaard 1999)). While it may be possible for the probes to be in the wakes of the anemometers when there is strong cross-wind, the pressure fluctuations due to the wake would be at frequencies much higher than the frequency range of the transducers, thus having negligible effect on the pressure measurements.

The pressure probes are modified commercial versions of the quad-disc design by Nishiyama & Bedard (1991), which are insensitive to velocity fluctuations and are capable of measuring pressure covariances with reasonable accuracy (Wyngaard, Siegel & Wilczak 1994). Each probe is connected through approximately 2 m of 1/4 inch (inner diameter) flexible tubing to a differential pressure transducer (Paroscientific Model 202BG). Attenuation of pressure fluctuations in the tubing is expected to be negligible (Lenschow & Raupach 1991). The 202BG is a bidirectional (dual-bellows) gauge pressure transducer with high resolution and accuracy, well-suited for turbulent pressure measurements in the surface layer. Movement of the bellows is of the order of 10^{-5} mm so that the induced pressure on the reference side of the transducer is negligible. The reference side of the transducers is connected to a common reference reservoir through thin 1/16 inch flexible tubing. Following Wilczak & Bedard (2004), the reference reservoir is filled with loosely packed steel wool and buried (approximately 0.3 m deep) to prevent generation of dynamic pressure from convection and to maintain a uniform temperature (and, hence, pressure) through conduction. However, due to persistent low-frequency pressure fluctuations within the reference system induced by radiative heating and advective cooling of the reference tubing, an additional transducer was added to measure the reference pressure using a second reference reservoir buried at the same depth as the first. The absolute pressure is obtained by adding the reference pressure back to the measured (probe) pressure. This pressure signal still contains some residual low-frequency fluctuations (less than 0.05 Hz). Because the lengths of the reference tubes (10–15 m) do not support acoustic waves of such low frequencies, these fluctuations have the same phase and affect the signals of all of the pressure transducers the same way. The fluctuations were found to affect the pressure terms in the Reynolds stress budget as well as those in the SGS stress budgets for very large filter widths ($\Lambda_w/\Delta_f < 1$). Thus, we only obtain the SGS pressure terms for $\Lambda_w/\Delta_f > 1$.

The sonic anemometer data are sampled at 60 s^{-1} and were rotated to correct for sonic anemometer tilt using the planar fit technique (Wilczak, Oncley & Stage 2001). The pressure data are sampled at 10 s^{-1} and then up-sampled to 60 s^{-1} using spectral interpolation to match the sampling rate of the sonic anemometers. Upsampling of the pressure signal avoids downsampling of the velocity and temperature signals and potential underestimation of the related statistics. It does not affect the pressure-related SGS statistics; a comparison of the results obtained using the two sampling rates shows negligible differences. Following Horst *et al.* (2004), we rotate the coordinate system and interpolate the velocity, temperature and pressure in the Cartesian coordinate system defined by the mean along-wind and cross-wind directions to obtain the virtual arrays (figure 1*a*). The interpolation is performed in spectral space to avoid attenuating the high-frequency (wavenumber) fluctuations. The coordinate rotation results in a decrease in the cross-wind spacing of the sensors, and therefore the effective filter width, by a factor of $\cos\alpha$, where α is the mean wind direction relative to the array normal. Following Wilczak & Bedard (2004), we also time-lag the pressure data using Taylor's hypothesis to account for the 29 cm separation between the pressure probe and sonic anemometer in the along-wind direction. This reduces the loss of scalar flux covariance (Kristensen *et al.* 1997). No correction was applied for the cross-wind separation of the sensors.

In the present study, we use the arrays to approximate top-hat filters. In the streamwise direction, assumption of Taylor's hypothesis (Lumley 1965) allows us to use the time-filtered signal as a surrogate for streamwise spatial filtering. Filtering in the transverse direction is performed by weight-averaging the output of the sensor

array (Tong *et al.* 1998). For example, the transversely filtered resolvable-scale velocity (denoted by a superscript t) is obtained as

$$u_i^t(\boldsymbol{x}, t) = \sum_{j=-N}^{N} C_j u_i(x_1, x_2 + j \times d, x_3, t), \qquad (2.1)$$

where $2N + 1$, C_j and d are the number of sensors on the array, the weighting coefficient for the jth sensor and the spacing between adjacent sensors, respectively. Owing to the limited number of sensors in the horizontal arrays, the weighting coefficients are chosen such that the response function of the low-resolution spanwise filter best matches that of the high-resolution streamwise filter (Horst *et al.* 2004). Streamwise and spanwise derivatives are approximated using fourth-order central finite-difference schemes, with a uniform spacing of $12\delta x = 12\delta y = 12d_y \cos \alpha$. Vertical derivatives are approximated using a first-order one-sided finite difference, with a spacing of $\delta z = z_s - z_p$.

Several previous works have investigated the array filtering technique, including the accuracy of two-dimensional filtering and use of Taylor's hypothesis. Using a spectral cutoff array filter, Tong *et al.* (1998) showed that the r.m.s. values of the filtered variables differed from that of a true spectral cutoff filter by less than 10 %. The accuracy of the top-hat array filter is expected to be higher (Chen & Tong 2006). They also showed two-dimensional filtering to be a good approximation of three-dimensional filtering with a 10–14 % higher variance. Field measurements by Higgins, Parlange & Meneveau (2007) confirmed this result and showed that the difference can be interpreted as a 16 % reduction in the filter size. Tong *et al.* (1998) showed that among the mechanisms that could affect the accuracy of Taylor's hypothesis, including the effects of different convecting velocities for different wavenumber components, temporal changes in the reference moving with the mean velocity and the fluctuating convecting velocity, only the last was significant. Higgins *et al.* (2012) showed that Taylor's hypothesis is more applicable to large-scale motions than small-scale motions in the surface layer. The errors associated with approximating gradients by finite differences were studied by Kleissl *et al.* (2003). They evaluated the divergence-free condition for the filtered velocity field using fourth- and first-order finite difference schemes for the horizontal and vertical derivatives, respectively, and concluded that the errors were acceptable for studying the SGS dynamics. Horst *et al.* (2004) further examined various issues of using the array technique, including the aliasing errors associated with evaluating derivatives using finite differences, and furthermore demonstrated reasonable accuracy of the technique.

Five different array configurations, shown in table 1, are employed in AHATS in order to vary the filter (grid) aspect ratio, z/Δ_f, and the stability parameter, z/L, where z, Δ_f and $L = -u_*^3 \Theta/(\kappa g \langle u_3' \theta' \rangle)$ are the height above the ground, the filter width and the Monin–Obukhov length, respectively, with primes denoting fluctuations and angle brackets denoting ensemble averaging. We refer to z as the height of the primary array z_p here and hereinafter. Note, $\kappa = 0.41$, $u_* = (-\langle u_1' u_3' \rangle)^{1/2}$ (with u_1' in the mean wind direction), and $\langle u_3' \theta' \rangle = Q_0$ are the von Kármán constant (Pope 2000), the friction velocity and the vertical temperature flux, respectively. We also define the surface-layer temperature scale as $T_* = -Q_0/u_*$. In the present work, we study the unstable surface layer (i.e. for which $z/L < 0$) using data from the medium and wide array configurations. We use 26 data segments, with each segment generally 30–90 min in length (most over 60 min), collected during the daytime and spanning a wide range of $-z/L$ (figure 2). Each data segment has a steady mean velocity and
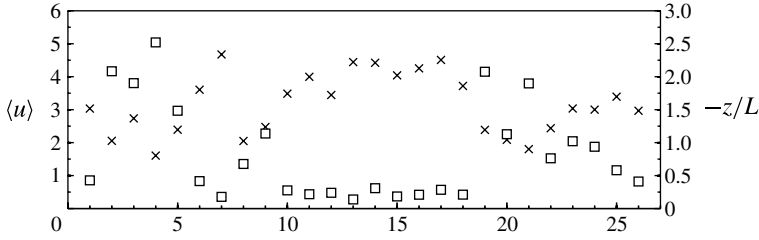
FIGURE 2. Measured mean wind velocity ($\times$) and surface layer stability ($\square$) for the 26 datasets used in the analyses.

Array	($\Delta_f = 2d_y$)	($\Delta_f = 4d_y$)	($\Delta_f = 6d_y$)	($\Delta_f = 8d_y$)
Wide 2	0.41	0.20	0.14	0.10
Medium 1	1.41	0.71	0.47	0.35
Medium 2	1.87	0.94	0.62	0.47

TABLE 2. The filter (grid) aspect ratio, z/Δ_f, for three-, five-, seven- and nine-point cross-wind filter widths; z refers to the height of the primary array z_p.

approximately stationary fluctuating velocities. The temperature data were detrended to remove any linear trend. The lengths for most datasets correspond to approximately 2000 advection time scales of the vertical-velocity energy-containing eddies. In this work the Reynolds-averaged statistics involve both time and spatial (across the array) averaging while the SGS statistics involve only time averaging. Although the precise level of statistical uncertainty is difficult to determine for some of the statistics obtained, it is sufficiently low for determining the dependence of the statistics on the important parameters (see § 3). Figure 3 gives the measured normal Reynolds stress components, friction velocity and vertical temperature flux for the 26 datasets used in the analyses. The resolved fields are obtained using four different filter widths. In the y direction, top-hat filters of width $\Delta_y = 2d_y$, $4d_y$, $6d_y$ and $8d_y$ are created from a weighted sum of three-, five-, seven- and nine-point cross-wind measurements, respectively. In the x direction, we use the mean wind velocity and sample rate to determine the streamwise filter width Δ_x (i.e. the number of data points in the averaging window) such that $\Delta_x = \Delta_y$. Shown in table 2, the filter aspect ratio z/Δ_f ranges from 0.10 to 1.87, allowing for the effects of grid anisotropy to be examined.

3. Results

In the present study, we examine the dynamics of the SGS stress and scalar flux and their dependence on the stability condition of the surface layer and the filter width through the budgets of the SGS TKE, the SGS stress and the SGS potential temperature flux. We investigate the dependence of the various terms in the SGS budgets on two non-dimensional parameters, z/L and Λ_w/Δ_f, where Λ_w is the wavelength corresponding to the peak of the vertical velocity spectrum. The dimensionless height, z/L, is a measure of the stability of the surface layer. The wavelength–filter-width ratio, Λ_w/Δ_f, is a measure of the resolution of the filter
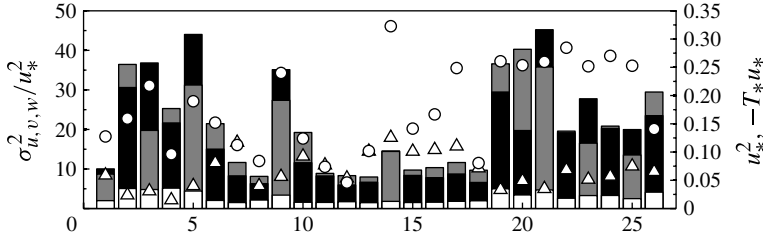
FIGURE 3. Measured Reynolds stress components (σ_u^2: top of black bars, σ_v^2: top of grey bars, σ_w^2: white bars), u_*^2 ($\triangle$) and $-T_* u_*$ ($\bigcirc$) for the 26 datasets used in the analyses.

relative to the turbulence field (i.e. a large value of Λ_w/Δ_f corresponds to a filter width much smaller than the energy-containing scales, and therefore a well-resolved LES field). Following Sullivan *et al.* (2003), we assume that $\Lambda_w = 2\pi U t_f$ (where U and t_f are the mean velocity in the along-wind direction and the Eulerian integral time scale, respectively) using Taylor's hypothesis, and determine t_f by fitting an exponential of the form $\rho(t) = \exp(-t/t_f)$ to the autocorrelation function of the vertical velocity (Lenschow, Mann & Kristensen 1993; Kaimal & Finnigan 1994).

In our analysis, the budget terms are non-dimensionalized using surface-layer scales u_*, Q_0 and z. Note that this differs from the study of Ramachandran & Wyngaard (2011), in which the terms in the budget of the deviatoric SGS stress are scaled by the energy dissipation rate (which is a function of the surface-layer stability and therefore collapse the budget for all $z/L \leqslant 0$ when used as the scaling parameter).

In the following we plot the budget terms against Λ_w/Δ_f for three ranges of z/L. Because the data span a range of z/L, one-dimensional curve fits do not accurately represent the results. To obtain curves for different values of z/L, we least-squares fit a surface (as a function of Λ_w/Δ_f and z/L) to all available data. We then obtain one-dimensional slices of the surface for chosen values of z/L. This method ensures that the overall dependence of the data on both parameters is well-determined. For very large filter widths, the magnitudes of the SGS stress and flux should approach those of the Reynolds stress and flux. Therefore, the values of the curves for $\Lambda_w/\Delta_f = 0$ are obtained from previous results in the literature (e.g. the budgets of the total TKE from Wyngaard (1971) and those of the Reynolds shear stress and temperature flux from Wyngaard, Coté & Izumi (1971)).

3.1. *SGS stress and flux*

Before analysing their budgets, we first present the results for the mean SGS stress and temperature flux. The mean SGS stress is shown in figure 4 as a function of Λ_w/Δ_f for the weakly, moderately and strongly convective surface layers. The SGS stress components have the largest magnitude near $\Lambda_w/\Delta_f = 0$ and decrease with increasing Λ_w/Δ_f (decreasing filter width). The normal components of $\langle \tau_{ij} \rangle$ show a clear dependence on the stability condition of the surface layer and increase with $-z/L$. The shear stress also generally increases with surface layer instability, however its dependence on z/L is weak. For very large filter widths, $\langle \tau_{11} \rangle > \langle \tau_{22} \rangle > \langle \tau_{33} \rangle$. The ratio of the mean horizontal SGS stress components to that of the vertical component (not shown) decreases with increasing $-z/L$. It also appears to decrease with increasing Λ_w/Δ_f (decreasing filter width).

The level of anisotropy of the SGS stress can be characterized using the Lumley triangle (Lumley 1978). Here, the two invariants, ξ and η, of the normalized
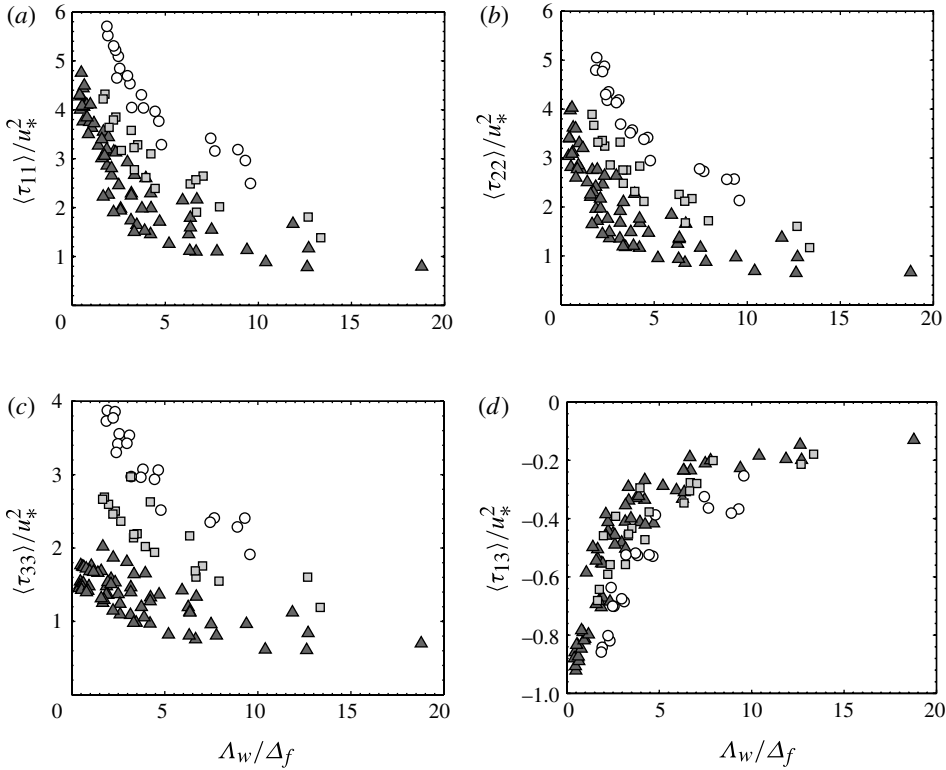
FIGURE 4. Measured mean SGS stress components for the weakly ($\blacktriangle$: $0 < -z/L \leqslant 0.8$), moderately ($\square$: $0.8 < -z/L \leqslant 1.5$) and strongly convective ($\bigcirc$: $-z/L > 1.5$) surface layers.

anisotropy tensor

$$b_{ij} = \frac{\langle \tau_{ij} \rangle}{\langle \tau_{kk} \rangle} - \frac{1}{3}\delta_{ij} \tag{3.1}$$

defined by Pope (2000),

$$6\xi^3 \equiv 3\mathrm{III}_b = b_{ii}^3 = b_{ij}b_{jk}b_{ki}, \tag{3.2}$$

$$6\eta^2 \equiv -2\mathrm{II}_b = b_{ii}^2 = b_{ij}b_{ji}, \tag{3.3}$$

are used. The invariants computed from the eigenvalues of the measured Reynolds and SGS stresses are shown in figure 5 as functions of Λ_w/Δ_f and z/L. In the left half of the Lumley triangle, the shape of the stress ellipsoid is a prolate spheroid (one small eigenvalue). In the right half, the stress ellipsoid is an oblate spheroid (one large eigenvalue). Sullivan *et al.* (2003) found the mean SGS stress in the weakly convective, neutral and weakly stable surface layers (most of their data lying within $-0.5 \leqslant z/L \leqslant 0.5$) to be generally axisymmetric with one large eigenvalue. Our results for the near-neutral and convective surface layers show that the Reynolds stress is generally axisymmetric with one small eigenvalue because, for the convective surface layer, the variances of the u and v velocity components are much larger than that of the w component. The data points also appear to move closer to $\eta = -\xi$
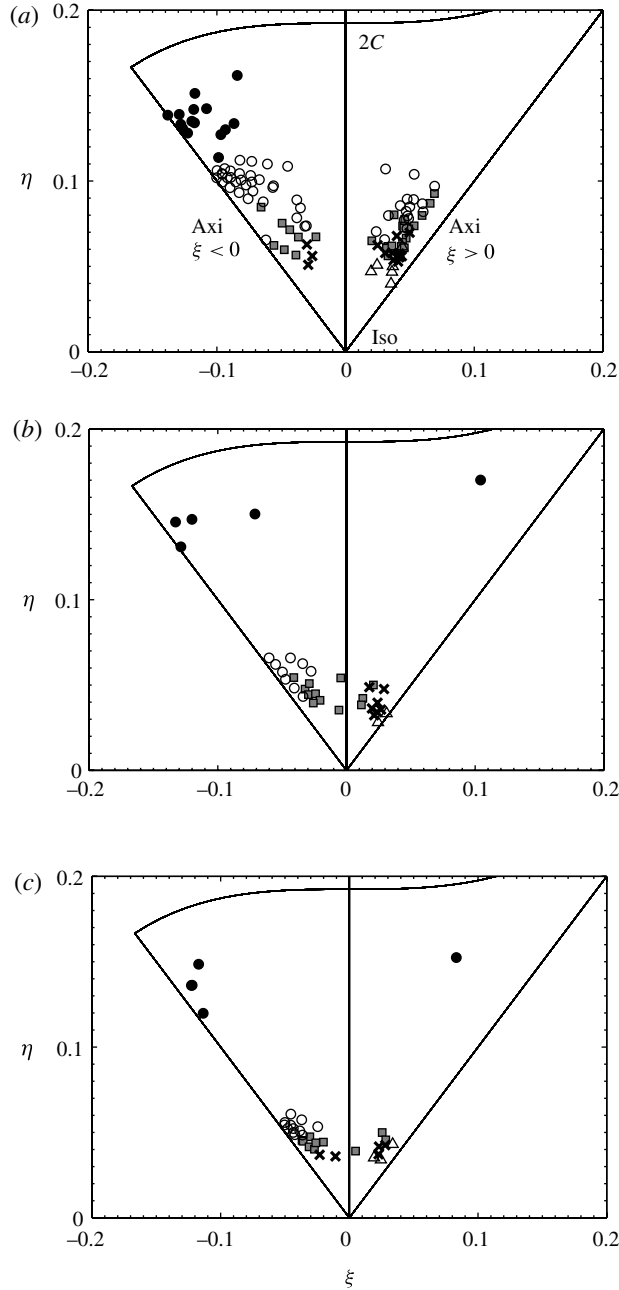
FIGURE 5. Lumley invariants of the mean Reynolds and SGS stress tensors for the (*a*) weakly ($0 < -z/L \leqslant 0.8$), (*b*) moderately ($0.8 < -z/L \leqslant 1.5$) and (*c*) strongly convective ($-z/L > 1.5$) surface layers: ●, Reynolds stress; ○, $0 < \Lambda_w/\Delta_f \leqslant 2$; ■, $2 < \Lambda_w/\Delta_f \leqslant 4$; ×, $4 < \Lambda_w/\Delta_f \leqslant 8$; △, $8 < \Lambda_w/\Delta_f \leqslant 20$.

as $-z/L$ increases since the Reynolds stress becomes more horizontally isotropic. The results for the SGS stress at large filter widths also follow this trend, with a stronger bias towards axisymmetric turbulence ($\xi < 0$) for increasing $-z/L$. For these
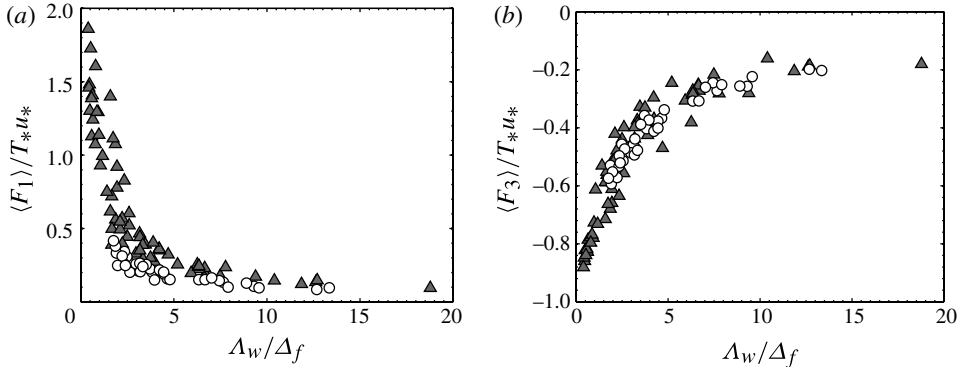
FIGURE 6. Measured mean SGS temperature flux components for the weakly (▲: $0 < -z/L \leqslant 1$) and strongly convective (○: $-z/L > 1$) surface layers.

filter widths, the level of anisotropy is stronger in the weakly convective surface layer. Since the peak of the u and v spectra occur at lower wavenumbers than that of the w spectrum (Kaimal *et al.* 1972), the filter affects mainly $\langle \tau_{11} \rangle$ and $\langle \tau_{22} \rangle$. The effects become stronger with increasing $-z/L$ since the spectral peaks for the u and v components move to lower wavenumbers; therefore the level of anisotropy decreases. As the filter width decreases, $\langle \tau_{11} \rangle$ and $\langle \tau_{22} \rangle$ fall off much faster than $\langle \tau_{33} \rangle$, but $\langle \tau_{11} \rangle > \langle \tau_{22} \rangle$; therefore the SGS stress tends toward axisymmetric turbulence with one large eigenvalue. The transition from one small eigenvalue to one large eigenvalue appears to occur at $2 \leqslant \Lambda_w/\Delta_f \leqslant 4$ and $4 \leqslant \Lambda_w/\Delta_f \leqslant 8$ for the moderately and strongly convective cases, respectively. For very small filter widths, the SGS stress should tend towards isotropy.

The mean SGS potential temperature flux is shown in figure 6 as a function of Λ_w/Δ_f for the weakly and strongly convective surface layers. Note that the non-dimensionalized fluxes have the opposite sign relative to the actual fluxes since $T_* < 0$ for unstable surface layers. The results show that the SGS temperature flux has the largest magnitude near $\Lambda_w/\Delta_f = 0$ and decreases with increasing Λ_w/Δ_f. The horizontal temperature flux, $\langle F_1 \rangle$, shows a clear dependence on z/L and decreases with increasing instability, while the vertical flux, $\langle F_3 \rangle$, appears to be independent of z/L. For the near-neutral surface layer, $\langle F_1 \rangle$ is nearly twice the magnitude of $\langle F_3 \rangle$. However, as $-z/L$ increases, $\langle F_1 \rangle$ should vanish as the local free convection condition is approached (Wyngaard *et al.* 1971).

3.2. *SGS TKE budget*

In this section, we discuss the results for the various terms in the budget of the SGS TKE. The budget terms are non-dimensionalized by $\kappa z/u_*^3$. Assuming nominal horizontal homogeneity of the field site (i.e. that mean quantities vary only in the vertical direction), the turbulent transport and pressure transport terms are treated as non-zero only in the vertical direction. The SGS TKE budget equation (1.10) thus reduces to

$$0 = \frac{1}{2}\frac{\partial}{\partial x_3}\langle T_{ii3}^{(t)} \rangle + \langle \mathscr{P} \rangle + \langle \mathscr{P}_B \rangle + \frac{1}{2}\frac{\partial}{\partial x_3}\langle T_{ii3}^{(p)} \rangle - \langle \epsilon \rangle. \qquad (3.4)$$

Here, the viscous transport term is small and has been neglected, and $\langle \epsilon_{ks} \rangle$ is approximated by $\langle \epsilon \rangle$ since the filter scale is much larger than the Kolmogorov
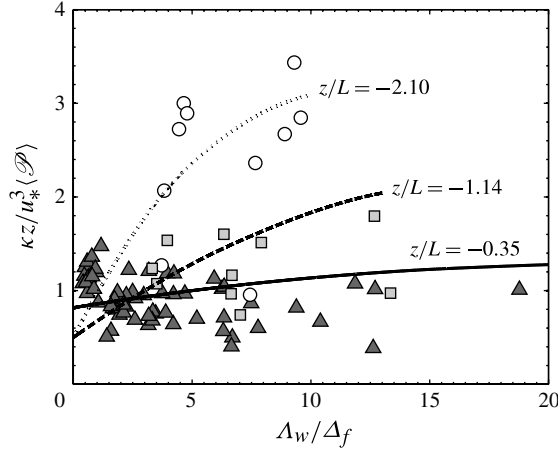
FIGURE 7. Non-dimensional mechanical production rate of SGS TKE as a function of Λ_w/Δ_f and z/L. The data are grouped into weakly (▲: $0 < -z/L \leqslant 0.8$), moderately (□: $0.8 < -z/L \leqslant 1.5$) and strongly convective (○: $-z/L > 1.5$) cases. The z/L value shown for each curve is the weight-averaged value for each stability group.

scale. We approximate the non-dimensional energy dissipation rate as $\kappa z \langle \epsilon \rangle / u_*^3 = -(1 + 0.75 \, | z/L |^{2/3})^{3/2}$ as suggested by Caughey & Wyngaard (1979). The individual budget terms are presented separately in figure 7–figure 10 to emphasize their dependencies on Λ_w/Δ_f and z/L. We then show a summary of the TKE budget in figure 11.

The non-dimensional mechanical production rate of the SGS TKE, $\kappa z \langle \mathscr{P} \rangle / u_*^3$, is shown in figure 7. The values of the curves for very small and very large Λ_w/Δ_f are based on the total TKE production rate and the dissipation rate, respectively. Here we use the mechanical production rate of the total TKE from Wyngaard (1971) to determine the values of the curves for $\Lambda_w/\Delta_f = 0$. For neutral surface layers, mechanical production and viscous dissipation are the dominant terms in the TKE budget. Therefore, in the limit as $-z/L$ and Λ_w/Δ_f approach zero, the mechanical production rate of the SGS TKE should approach that of the total TKE with a normalized value of $\kappa z \langle \mathscr{P} \rangle / u_*^3 = 1$. For unstable surface layers, the mechanical production rate for very small values of Λ_w/Δ_f should decrease with increasing $-z/L$ because the mean shear is weakened by the large convective eddies sweeping the surface layer (energy is also gained through buoyant production and pressure transport). As Λ_w/Δ_f increases (filter width decreases), the mechanical production rate for the unstable surface layers should increase as the energy gained by the resolvable scales due to buoyant production and pressure transport is increasingly cascading down to the subgrid scales through spectral transfer (i.e. the SGS mechanical production). It also increases with $-z/L$ because more energy enters the cascade due to the higher buoyant production and pressure transport at large scales. For very large values of Λ_w/Δ_f, the TKE budget reduces to a balance between the SGS production and viscous dissipation.

The buoyant production rate of the SGS TKE, shown in figure 8, is a gain in the unstable surface layer and increases with $-z/L$. For very small values of Λ_w/Δ_f (very large filter widths), the buoyant production rate of the SGS TKE should approach that of the total TKE and hence scale with the stability parameter. For each stability
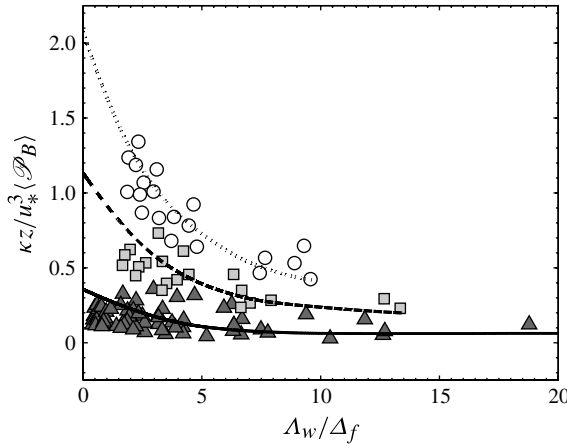
FIGURE 8. Non-dimensional buoyant production rate of SGS TKE as a function of Λ_w/Δ_f and z/L. The data are grouped as in figure 7.
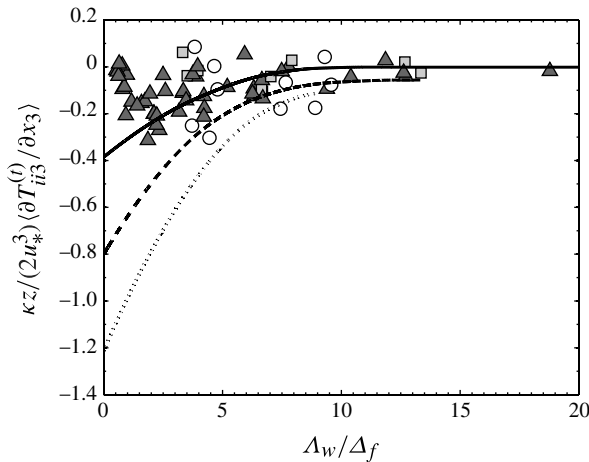

FIGURE 9. Non-dimensional turbulent transport rate of SGS TKE as a function of Λ_w/Δ_f and z/L. The data are grouped as in figure 7.

range, it has the maximum magnitude at $\Lambda_w/\Delta_f = 0$ and monotonically decreases with the filter width since buoyancy has a diminishing effect on the smaller SGS eddies (Wyngaard 2004).

Turbulent transport (shown in figure 9) exports energy upward, and therefore is a loss in the SGS TKE budget. The results for the weakly unstable surface layer and large filter widths agree with Wyngaard *et al.* (1971), although the scatter is somewhat larger. This may be due to the errors involved in approximating vertical derivatives using one-sided finite differencing, in addition to the statistical uncertainties in computing third-order moments. In general, the rate of turbulent transport increases with $-z/L$ due to the stronger thermal plumes transporting energy upward. Similar to the buoyant production, it has the maximum magnitude at $\Lambda_w/\Delta_f = 0$ and decreases with increasing Λ_w/Δ_f (decreasing filter width), asymptotically approaching zero for
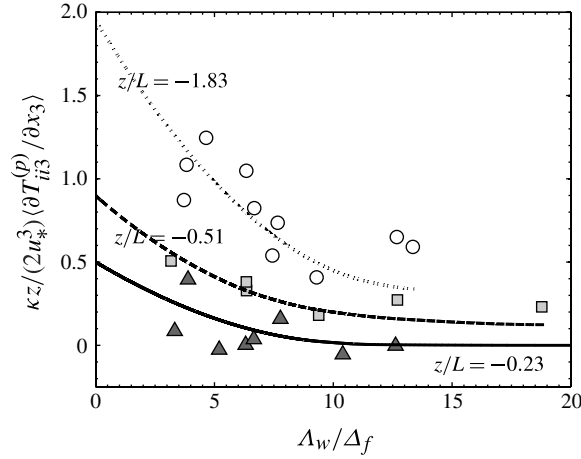
FIGURE 10. Non-dimensional pressure transport rate of SGS TKE for the weakly (▲: $0 < -z/L \leqslant 0.3$), moderately (▨: $0.3 < -z/L \leqslant 1$) and strongly convective (○: $-z/L > 1$) surface layers.

large values of Λ_w/Δ_f since transport has a diminishing effect on the smaller SGS eddies.

The rate of pressure transport of the SGS TKE is shown in figure 10 for three ranges of z/L (due to the amount of pressure data available, the mean stability values here differ from those of the previous figures). The pressure transport is a gain in the budget of the SGS TKE and increases with $-z/L$, while its magnitude has a trend similar to that of the SGS turbulent transport. In the limit as Λ_w/Δ_f approaches zero, the SGS pressure transport should approach that of the total TKE. So we compare our results with those of the total TKE budget obtained in previous studies: for near-neutral surface layers, the pressure transport is small and the primary source of energy is mechanical production (fed by the mean flow). For convective surface layers, our results show that the pressure transport is a major gain in the budget of the SGS TKE. Numerous studies have inferred the magnitude of the pressure transport term in the budget of the total TKE (e.g. Wyngaard & Coté 1971; McBean & Elliott 1975; Bradley, Antonia & Chambers 1981; Wilczak & Businger 1984), showing that it nearly balances the rate of turbulent transport for unstable surface layers. The magnitude of the pressure term inferred in these studies agree closely with those in figure 10 (for small values of Λ_w/Δ_f) for the given values of z/L. The trends in figure 10 for large values of Λ_w/Δ_f also agree with Elliott (1972), who analysed microscale pressure fluctuations measured within the ABL. He showed that large-scale pressure fluctuations are approximately in phase with downward velocity fluctuations, whereas, for small scales, there is a large phase difference. This was argued to be the result of the large eddies interacting with the surface and the small scales being 'free' from the effects of the ground. Thus, as Λ_w/Δ_f increases, the rate of pressure transport should decrease and asymptotically approach zero as the smaller SGS eddies are less affected by the free surface.

To summarize the SGS TKE budget we show in figure 11 all of the terms discussed above. We plot the rate of viscous dissipation as a horizontal line since it is independent of Λ_w/Δ_f. For neutral surface layers, similar to the total TKE budget we expect an approximate balance between the mechanical production and the viscous
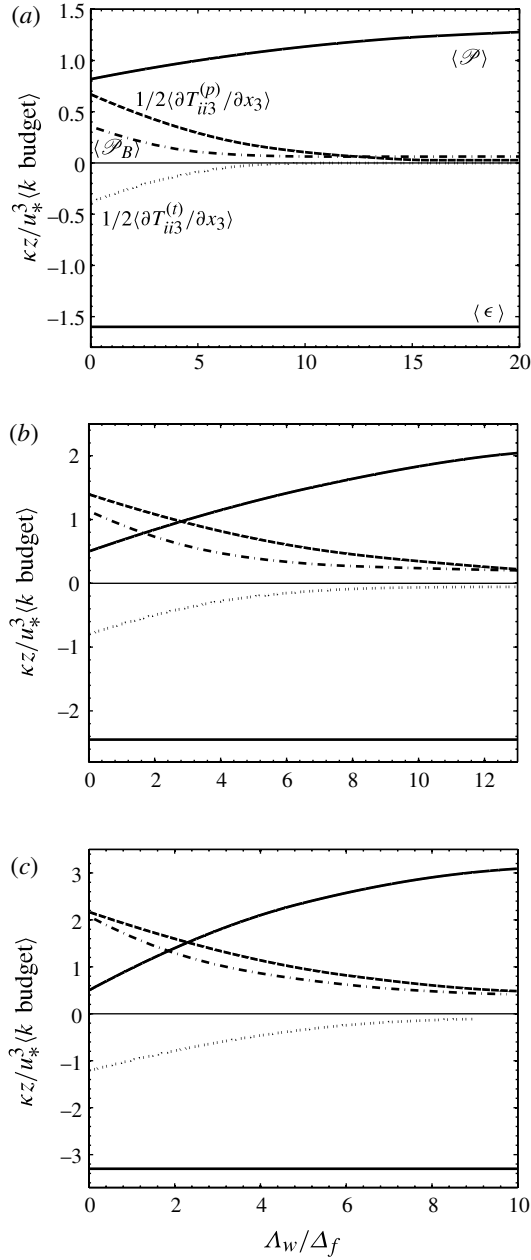
FIGURE 11. Summary of the SGS TKE budget as a function of Λ_w/Δ_f for (a) $z/L = -0.35$, (b) $z/L = -1.14$ and (c) $z/L = -2.10$.

dissipation for the SGS TKE budget. For near-neutral surface layers (figure 11a), the buoyant production, the SGS turbulent transport and the SGS pressure transport begin to contribute to the budget. For unstable surface layers (figures 11b,c), the mechanical production, the buoyant production and the SGS pressure transport are balanced by the SGS turbulent transport and the viscous dissipation for large filter widths. As

the filter width decreases, the buoyancy and transport terms become less significant, and the budget is reduced to a balance between the mechanical production (spectral transfer) and the viscous dissipation, both increasing with $-z/L$. The magnitude and trends of each term, notably the gain by the SGS pressure transport under unstable conditions, are consistent with those of the total TKE summarized by Högström (1990) and Wyngaard (1992). The sum of the measured mechanical production, buoyant production and SGS pressure transport balances the sum of the SGS turbulent transport and the viscous dissipation to within 10 % of their magnitudes.

3.3. *SGS stress budgets*

In this section, we discuss the results for the various terms in the budgets of the SGS stress components. Owing to the nominal horizontal homogeneity of the field site, the pressure transport terms in the budgets of $\langle \tau_{11} \rangle$ and $\langle \tau_{22} \rangle$ are assumed to be zero. Hence, the SGS velocity–pressure-gradient correlation terms are equal to the SGS pressure–strain-rate correlations. Likewise, turbulent transport is non-zero only in the vertical direction. The budget equation (1.1) for $\langle \tau_{\alpha\alpha} \rangle$ ($\alpha = 1, 2$; no summation) thus reduces to

$$0 = \frac{\partial}{\partial x_3} \langle T^{(t)}_{\alpha\alpha 3} \rangle + \langle P_{\alpha\alpha} \rangle + \langle \mathcal{R}_{\alpha\alpha} \rangle - \langle \epsilon_{\alpha\alpha} \rangle, \qquad (3.5)$$

where the viscous transport term in (1.1) has been neglected and $\langle \epsilon_{s\alpha\alpha} \rangle$ is approximated as $\langle \epsilon_{\alpha\alpha} \rangle = 2\nu \langle (\partial u_\alpha / \partial x_k)^2 \rangle$. The budget equations for $\langle \tau_{33} \rangle$ and $\langle \tau_{13} \rangle$ are

$$0 = \frac{\partial}{\partial x_3} \langle T^{(t)}_{333} \rangle + \langle P_{33} \rangle + \langle P_{B33} \rangle + \langle \mathcal{R}_{33} \rangle - \frac{\partial}{\partial x_3} \langle T^{(p)}_{333} \rangle - \langle \epsilon_{33} \rangle \qquad (3.6)$$

and

$$0 = \frac{\partial}{\partial x_3} \langle T^{(t)}_{133} \rangle + \langle P_{13} \rangle + \langle P_{B13} \rangle + \langle \Pi_{13} \rangle, \qquad (3.7)$$

respectively. The viscous transport and dissipation are small and are neglected in (3.7).

The budget of the SGS stress component $\langle \tau_{11} \rangle$, given by (3.5), includes the mechanical production, the turbulent transport, the pressure–strain-rate correlation and the dissipation. The mechanical production rate of $\langle \tau_{11} \rangle$, $\langle P_{11} \rangle$, is shown in figure 12. Note that for very small values of Λ_w / Δ_f (very large filter widths), $\langle \tau_{ij} \rangle$ should approach the Reynolds stress. Hence, for the near-neutral surface layer, $\langle P_{11} \rangle$ should approach a normalized value of $\kappa z \langle P_{11} \rangle / u_*^3 = 2$ (twice the production rate of the total TKE), thereby balancing the normalized dissipation rate ($\kappa z \langle \epsilon_{11} \rangle / u_*^3 = 2$). For very large values of Λ_w / Δ_f (very small filter widths), $\langle P_{11} \rangle$ essentially becomes the spectral transfer rate for $\langle \tau_{11} \rangle$, which equals two-thirds of the SGS TKE. Therefore, $\langle P_{11} \rangle$ should approach a normalized value of $(2/3)\kappa z \langle \epsilon \rangle / u_*^3 = 2/3$, the dissipation rate of $\langle \tau_{11} \rangle$ under neutral stability. For weakly convective surface layers, $\langle P_{11} \rangle$ decreases with increasing Λ_w / Δ_f (decreasing filter width). For moderately and strongly convective surface layers, $\langle P_{11} \rangle$ appears to increase with Λ_w / Δ_f; it also increases with $-z/L$. For these surface layers, $\langle P_{11} \rangle$ for very small Λ_w / Δ_f should be smaller than that under near-neutral conditions because the mean shear is weakened by the convective mixing. Again we use the results for the Reynolds stress obtained by Wyngaard (1971) to determine the values of the curves for $\Lambda_w / \Delta_f = 0$. For very large values of Λ_w / Δ_f, $\langle P_{11} \rangle$ becomes the spectral transfer rate, which is higher for unstable surface layers due
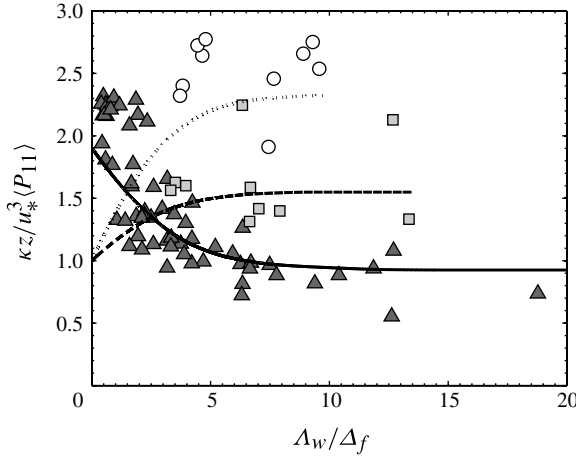
FIGURE 12. Non-dimensional production rate of $\langle \tau_{11} \rangle$ for the weakly ($\blacktriangle$: $0 < -z/L \leqslant 0.8$), moderately ($\square$: $0.8 < -z/L \leqslant 1.5$) and strongly convective ($\circ$: $-z/L > 1.5$) surface layers.
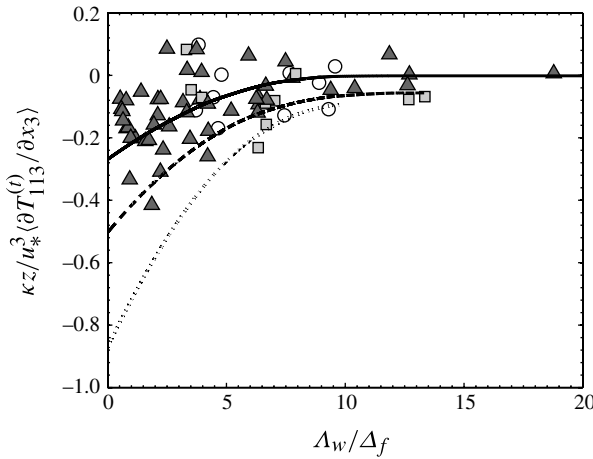

FIGURE 13. Non-dimensional turbulent transport rate of $\langle \tau_{11} \rangle$ as a function of Λ_w/Δ_f and z/L. The data are grouped as in figure 12.

to the high buoyant production rate of the resolvable scales, resulting in more energy cascading down to the subgrid scales. Hence, $\langle P_{11} \rangle$ is higher and increases with $-z/L$.

The rate of turbulent transport of $\langle \tau_{11} \rangle$, $\langle \partial T_{113}^{(t)}/\partial x_3 \rangle$, shown in figure 13, is a loss in the budget of $\langle \tau_{11} \rangle$. The results for the weakly unstable surface layer and $\Lambda_w/\Delta_f = 0$ agree well with Wyngaard & Coté (1971), although there is some scatter. In general, the magnitude of $\langle \partial T_{113}^{(t)}/\partial x_3 \rangle$ increases with increasing instability and decreases with decreasing filter width, asymptotically approaching zero for large values of Λ_w/Δ_f since the mentioned inhomogeneity has a diminishing effect on the smaller SGS eddies.

The SGS pressure–strain-rate correlation term in the budget of $\langle \tau_{11} \rangle$, $\langle \mathscr{R}_{11} \rangle$, is shown in figure 14. For near-neutral surface layers, the subgrid scales gain energy primarily
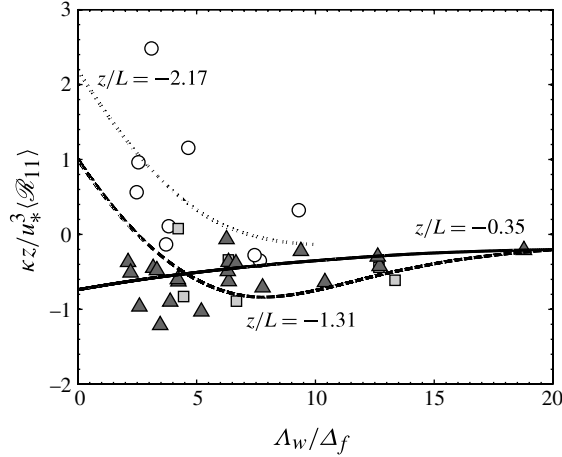
FIGURE 14. Non-dimensional SGS pressure–strain-rate correlation in the budget of $\langle \tau_{11} \rangle$ for the weakly ($\blacktriangle$: $0 < -z/L \leqslant 0.75$), moderately ($\square$: $0.75 < -z/L \leqslant 1.75$) and strongly convective ($\bigcirc$: $-z/L > 1.75$) surface layers.

through $\langle P_{11} \rangle$ (at large filter widths). Hence, for these surface layers, $\langle \mathscr{R}_{11} \rangle$ is a loss (negative), indicating that the pressure–strain-rate correlation is removing energy from $\langle \tau_{11} \rangle$ and redistributing it to the other normal SGS components ($\langle \tau_{22} \rangle$ and $\langle \tau_{33} \rangle$). It has the maximum magnitude at $\Lambda_w/\Delta_f = 0$. As Λ_w/Δ_f increases, $\langle P_{ij} \rangle$ and $\langle \tau_{ij} \rangle$ become less anisotropic; therefore, the magnitude of $\langle \mathscr{R}_{11} \rangle$ decreases and approaches zero for very large values of Λ_w/Δ_f. For moderately and strongly convective surface layers, $\langle \mathscr{R}_{11} \rangle$ is positive for small values of Λ_w/Δ_f because it is a major gain for the Reynolds stress component $\langle u_1' u_1' \rangle$. This is due to the surface blockage of the large, downward returning, convective eddies (e.g. Wyngaard 1992), resulting in energy being transferred from the vertical ($\langle \tau_{33} \rangle$) to the horizontal velocity components. For larger $-z/L$, buoyancy is more dominant; thus, the blockage effect is stronger and the energy being produced in the vertical direction is increasingly transferred to the horizontal components by the SGS pressure–strain-rate correlation, causing $\langle \mathscr{R}_{11} \rangle$ to increase (for small values of Λ_w/Δ_f). As Λ_w/Δ_f increases, the effects of the ground blockage and buoyancy are reduced for smaller eddies while the anisotropy in $\langle \tau_{ij} \rangle$ becomes relatively more important. Thus, $\langle \mathscr{R}_{11} \rangle$ reverses sign for moderate values of Λ_w/Δ_f, becoming a sink in the budget of $\langle \tau_{11} \rangle$ and acting to transfer energy back to $\langle \tau_{33} \rangle$. This transition (zero crossing) occurs approximately at $\Lambda_w/\Delta_f = 3$ and 8 for the moderately and strongly convective cases, respectively, consistent with the transition of the SGS stress from one small to one large eigenvalue (figure 5). For very large values of Λ_w/Δ_f, $\langle \tau_{ij} \rangle$ becomes increasingly isotropic, and hence we expect the effects of $\langle \mathscr{R}_{ij} \rangle$ to diminish and $\langle \mathscr{R}_{11} \rangle$ to approach zero. Thus, $\langle \mathscr{R}_{11} \rangle$ has a non-monotonic dependence on Λ_w/Δ_f for large values of $-z/L$.

To summarize the $\langle \tau_{11} \rangle$ budget for unstable surface layers, we show in figure 15 all of the budget terms as functions of Λ_w/Δ_f for $z/L = -2.10$. For very large filter widths, energy is supplied to $\langle \tau_{11} \rangle$ by the mechanical production and by the SGS pressure–strain-rate correlation (with energy transferred from $\langle \tau_{33} \rangle$), with the latter being the dominant source. These gains are balanced by the SGS turbulent transport and the viscous dissipation. As the filter width decreases, $\langle \mathscr{R}_{11} \rangle$ decreases and becomes negative before approaching zero for very small filter widths. The SGS

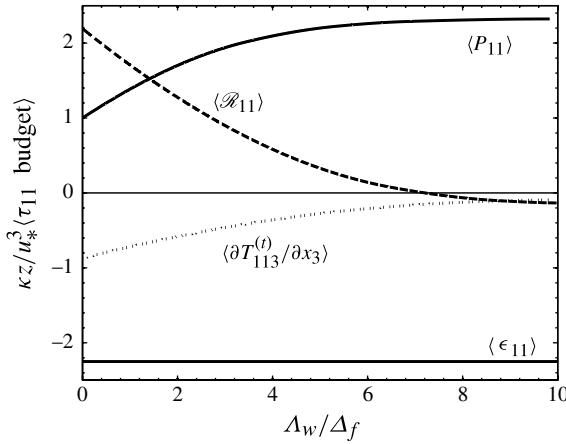FIGURE 15. Summary of the budget of $\langle \tau_{11} \rangle$ as a function of Λ_w/Δ_f for $z/L = -2.10$.
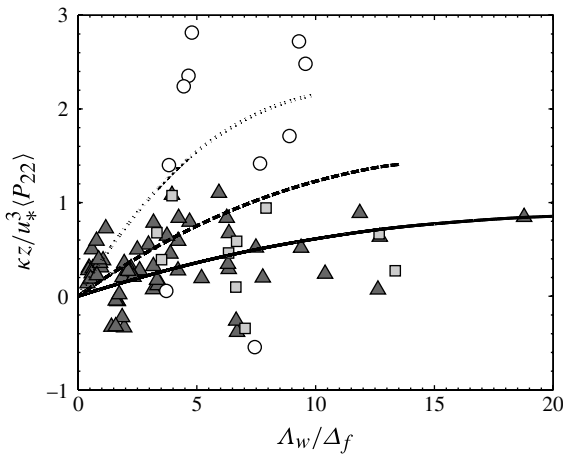

FIGURE 16. Non-dimensional production rate of $\langle \tau_{22} \rangle$ for the weakly ($\blacktriangle$: $0 < -z/L \leqslant 0.8$), moderately ($\blacksquare$: $0.8 < -z/L \leqslant 1.5$) and strongly convective ($\bigcirc$: $-z/L > 1.5$) surface layers.

turbulent transport also decreases (monotonically), resulting in a balance between the mechanical production and viscous dissipation. The imbalance of the terms in the budget is generally within 10 % of the sum of the gain (or loss) terms.

The budget of the SGS stress component $\langle \tau_{22} \rangle$, given by (3.5), includes the mechanical production, the pressure–strain-rate correlation, the turbulent transport and the viscous dissipation. The mechanical production rate of $\langle \tau_{22} \rangle$, $\langle P_{22} \rangle$, is shown in figure 16. In the limit as Λ_w/Δ_f approaches zero (very large filter widths), $\langle P_{22} \rangle$ should approach zero for all z/L since the production rate of the Reynolds stress component $\langle u_2' u_2' \rangle$ is zero due to the nominal horizontal homogeneity of the surface layer. Figure 16 shows that $\langle P_{22} \rangle$ increases with increasing Λ_w/Δ_f (decreasing filter width) and increasing instability. Similar to $\langle P_{11} \rangle$, for very large values of Λ_w/Δ_f (very small filter widths) $\langle P_{22} \rangle$ should approach the mean dissipation rate, $\langle \epsilon_{22} \rangle = (2/3)\langle \epsilon \rangle$.
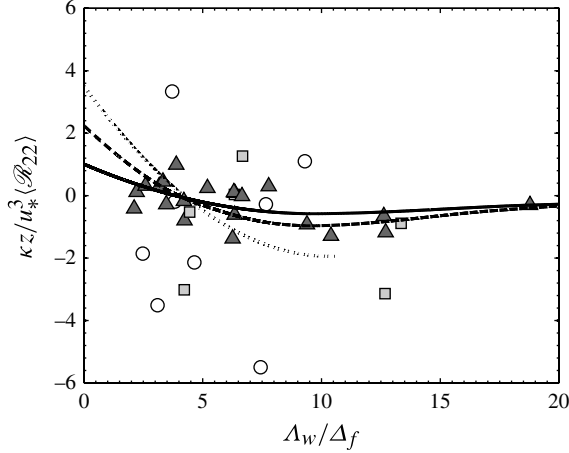
FIGURE 17. Non-dimensional SGS pressure–strain-rate correlation in the budget of $\langle \tau_{22} \rangle$ for the weakly (▲: $0 < -z/L \leqslant 0.75$), moderately (▣: $0.75 < -z/L \leqslant 1.75$) and strongly convective (○: $-z/L > 1.75$) surface layers.

The SGS pressure–strain-rate correlation term in the budget of $\langle \tau_{22} \rangle$, $\langle \mathscr{R}_{22} \rangle$, is shown in figure 17. For weakly unstable surface layers and large filter widths, $\langle \mathscr{R}_{22} \rangle$ is a gain since the pressure–strain-rate correlation redistributes energy from $\langle \tau_{11} \rangle$ and $\langle \tau_{33} \rangle$ to $\langle \tau_{22} \rangle$ (for the surface layers studied, both $\langle \mathscr{R}_{11} \rangle$ and $\langle \mathscr{R}_{33} \rangle$ are negative). As Λ_w/Δ_f increases, the anisotropy in $\langle \tau_{ij} \rangle$ becomes relatively more important, causing $\langle \mathscr{R}_{22} \rangle$ to become a sink in the budget of $\langle \tau_{22} \rangle$ as energy is transferred back to $\langle \tau_{33} \rangle$. These effects become stronger with increasing instability. For strongly convective surface layers and small Λ_w/Δ_f, $\langle \mathscr{R}_{22} \rangle$ is positive with a larger magnitude. Again this is a result of the larger convective eddies being blocked by the surface and of increasing buoyancy production and pressure transport in the vertical direction, causing energy transfer from the vertical to the horizontal velocity components. Thus, the magnitude of $\langle \mathscr{R}_{22} \rangle$ increases (positively) with increasing instability. However, as Λ_w/Δ_f increases, the effects of the surface and buoyancy are again reduced while the anisotropy in $\langle \tau_{ij} \rangle$ becomes relatively more important. Therefore, $\langle \mathscr{R}_{22} \rangle$ should reverse sign for moderate values of Λ_w/Δ_f, now becoming a loss in the budget of $\langle \tau_{22} \rangle$ and acting to drive $\langle \tau_{ij} \rangle$ towards isotropy. For very large values of Λ_w/Δ_f, we again expect $\langle \mathscr{R}_{22} \rangle$ to approach zero.

The budget of the SGS stress component $\langle \tau_{33} \rangle$, given by (3.6), includes the mechanical production, the buoyant production (same as that of the SGS TKE), the pressure–strain-rate correlation, the pressure transport (same as that of the SGS TKE), the turbulent transport and the viscous dissipation. The mechanical production rate of $\langle \tau_{33} \rangle$, $\langle P_{33} \rangle$, is shown in figure 18. For very small values of Λ_w/Δ_f (very large filter widths), the magnitude of $\langle P_{33} \rangle$ is small because the mean shear does not contribute to $\langle P_{33} \rangle$. For smaller filter widths, $\langle P_{33} \rangle$ should increase with increasing instability because more resolvable-scale energy is cascading down to the subgrid scales. Figure 18 shows that $\langle P_{33} \rangle$ also increases with increasing Λ_w/Δ_f (decreasing filter width) because the buoyant production is smaller, thus $\langle \tau_{33} \rangle$ relies more on the spectral transfer to supply energy. For very small filter widths, $\langle P_{33} \rangle$ should approach $\langle \epsilon_{33} \rangle = (2/3)\langle \epsilon \rangle$, thereby balancing the mean dissipation rate. The buoyant production rate, $\langle P_{B33} \rangle$, is the same as that of the total SGS TKE (figure 8, with twice the
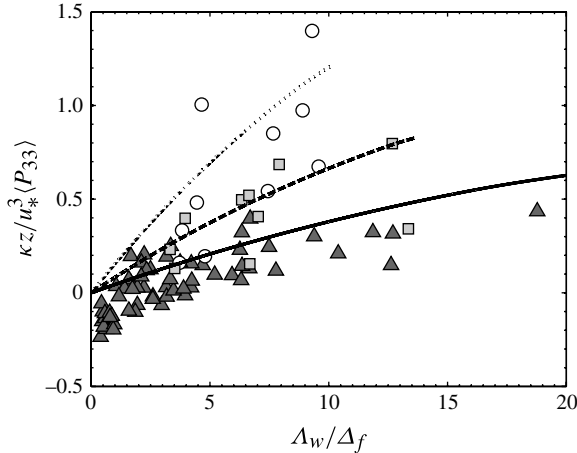
FIGURE 18. Non-dimensional production rate of $\langle\tau_{33}\rangle$ for the weakly (▲: $0 < -z/L \leqslant 0.8$), moderately (□: $0.8 < -z/L \leqslant 1.5$) and strongly convective (○: $-z/L > 1.5$) surface layers.

magnitude). For moderately and strongly convective surface layers, buoyant production is a major gain in the budget of $\langle\tau_{33}\rangle$ for large filter widths, with the magnitude of $\langle P_{B33}\rangle$ increasing with increasing $-z/L$. This energy being produced in the vertical direction is then transferred to the horizontal components by the pressure–strain-rate correlation. For small filter widths, mechanical production is the dominant gain in the budget of $\langle\tau_{33}\rangle$, while $\langle P_{B33}\rangle$ approaches zero.

The SGS pressure–strain-rate correlation term in the budget of $\langle\tau_{33}\rangle$, $\langle\mathscr{R}_{33}\rangle$, is shown in figure 19. For strongly convective surface layers, $\langle\mathscr{R}_{33}\rangle$ should be a sink in the budget of $\langle\tau_{33}\rangle$ for small values of Λ_w/Δ_f, again because energy is redistributed from $\langle\tau_{33}\rangle$ to $\langle\tau_{11}\rangle$ and $\langle\tau_{22}\rangle$. Here, energy gained in the vertical direction through buoyancy production and pressure transport is fed to the horizontal components by the pressure–strain-rate correlation as the vertical motion of the large convective eddies are blocked by the ground. As Λ_w/Δ_f increases, the anisotropy in $\langle\tau_{ij}\rangle$ becomes relatively more important than the effects of the ground blockage and buoyancy, causing $\langle\mathscr{R}_{33}\rangle$ to reverse sign and become positive ($\langle\tau_{33}\rangle$ now receiving energy from $\langle\tau_{11}\rangle$ and $\langle\tau_{22}\rangle$ through the pressure–strain-rate correlation). For very large values of Λ_w/Δ_f, we expect $\langle\mathscr{R}_{33}\rangle$ to approach zero as $\langle P_{33}\rangle$ becomes the main energy source. Hence, we expect $\langle\mathscr{R}_{33}\rangle$ to have a non-monotonic dependence on Λ_w/Δ_f under convective conditions. For neutral surface layers, $\langle\mathscr{R}_{33}\rangle$ should be positive (not shown) because it is the main energy source in the $\langle\tau_{33}\rangle$ budget. As Λ_w/Δ_f increases, $\langle\tau_{ij}\rangle$ becomes more isotropic, causing $\langle\mathscr{R}_{33}\rangle$ to decrease. For large values of Λ_w/Δ_f, we again expect $\langle\mathscr{R}_{33}\rangle$ to asymptotically approach zero as $\langle P_{33}\rangle$ becomes the dominant energy source.

The budget terms for $\langle\tau_{22}\rangle$ and $\langle\tau_{33}\rangle$ appear to have larger scatters and imbalances (typically 20–30 %) compared with 10 % for $\langle\tau_{11}\rangle$. However, the trends of the terms are consistent with each other and, for large filter widths, with those of the Reynolds stress. Thus, these differences do not affect the conclusions drawn from the results.

The budget of the SGS stress component $\langle\tau_{13}\rangle$, given by (3.7), is dominated by the shear production, the buoyant production and the velocity–pressure-gradient correlation (turbulent transport is small, while viscous dissipation is negligible due to local isotropy). The SGS shear production rate and buoyant production rate of $\langle\tau_{13}\rangle$, $\langle P_{13}\rangle$ and $\langle P_{B13}\rangle$, are shown in figures 20 and 21, respectively. For very small values
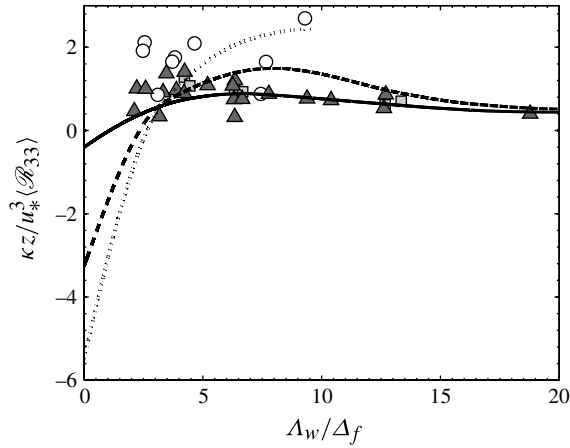
FIGURE 19. Non-dimensional SGS pressure–strain-rate correlation in the budget of $\langle \tau_{33} \rangle$ for the weakly (▲: $0 < -z/L \leqslant 0.75$), moderately (▢: $0.75 < -z/L \leqslant 1.75$) and strongly convective (○: $-z/L > 1.75$) surface layers.
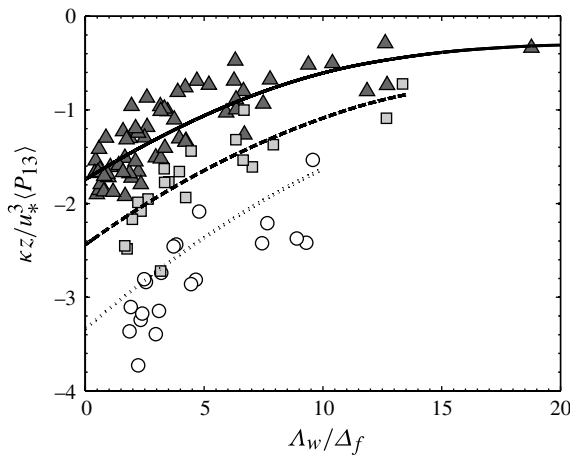

FIGURE 20. Non-dimensional shear production rate of $\langle \tau_{13} \rangle$ for the weakly (▲: $0 < -z/L \leqslant 0.8$), moderately (▢: $0.8 < -z/L \leqslant 1.5$) and strongly convective (○: $-z/L > 1.5$) surface layers.

of Λ_w/Δ_f, the magnitudes of $\langle P_{13} \rangle$ and $\langle P_{B13} \rangle$ should approach the shear production and buoyant production rates of the Reynolds shear stress, respectively. Here, we use the production rates of the Reynolds shear stress obtained by Wyngaard *et al.* (1971) to determine the values of the curves for $\Lambda_w/\Delta_f = 0$. Figure 20 shows that $\langle P_{13} \rangle$ decreases (smaller magnitude, since $\langle \tau_{13} \rangle$ is negative) with increasing Λ_w/Δ_f because the production tensor $\langle P_{ij} \rangle$ and the SGS stress become more isotropic for smaller filter widths. Consistent with the trends of the Reynolds shear stress, $\langle P_{13} \rangle$ also increases with $-z/L$. The trends of $\langle P_{B13} \rangle$ are similar to those of $\langle P_{13} \rangle$, but the magnitude is smaller. Here $\langle P_{B13} \rangle$ approaches zero for neutral surface layers and increases with
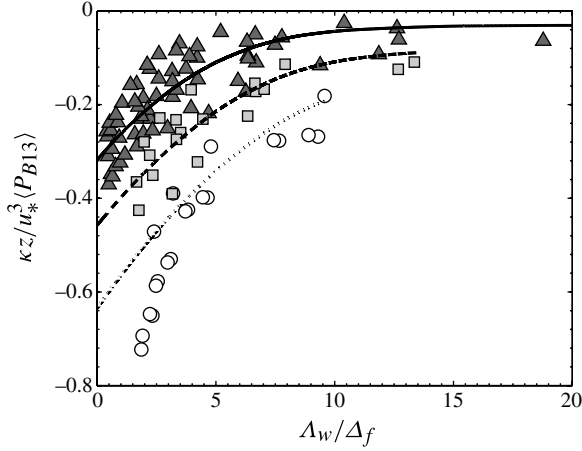
FIGURE 21. Non-dimensional buoyant production rate of $\langle \tau_{13} \rangle$ as a function of Λ_w/Δ_f and z/L. The data are grouped as in figure 20.
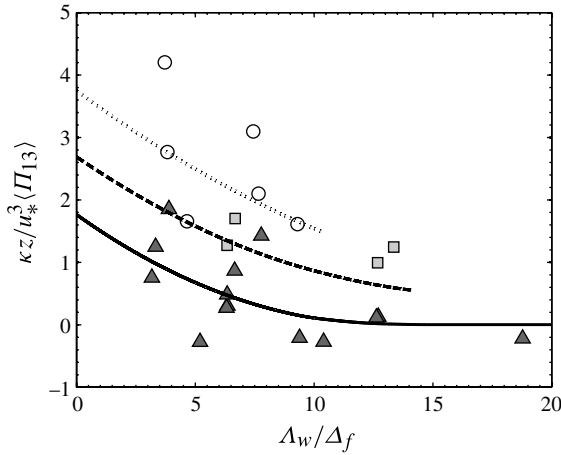

FIGURE 22. Non-dimensional SGS velocity–pressure-gradient correlation in the budget of $\langle \tau_{13} \rangle$ for the weakly (▲: $0 < -z/L \leqslant 0.75$), moderately (□: $0.75 < -z/L \leqslant 1.75$) and strongly convective (○: $-z/L > 1.75$) surface layers.

increasing $-z/L$. It monotonically decreases with increasing Λ_w/Δ_f (decreasing filter width).

The SGS velocity–pressure-gradient correlation, $\langle \Pi_{13} \rangle$, which combines the effects of the pressure–strain-rate correlation and the pressure transport, is generally positive (figure 22) and, hence, a loss in the shear stress budget. In the limit as Λ_w/Δ_f approaches zero, $\langle \Pi_{13} \rangle$ should approach the velocity–pressure-gradient correlation term in the budget of the Reynolds shear stress. Here, its trend and magnitude agree well with those inferred by Wyngaard *et al.* (1971). It monotonically decreases with increasing Λ_w/Δ_f (smaller filter width) and increases with increasing $-z/L$. The trends of $\langle \Pi_{13} \rangle$ generally counter those of $\langle P_{13} \rangle$ and $\langle P_{B13} \rangle$, thereby closing the quasi-steady shear stress budget. Thus, in a way similar to the Reynolds shear stress budget, the
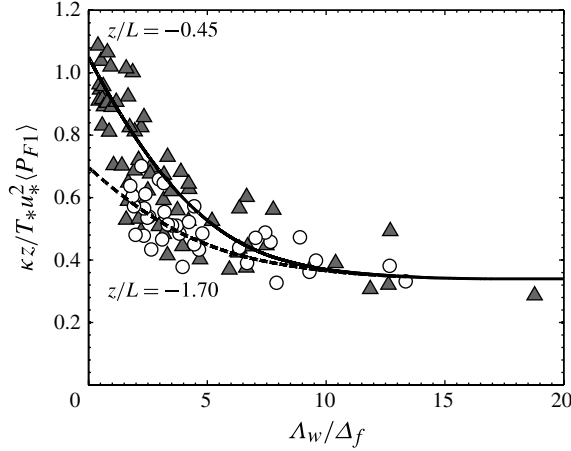
FIGURE 23. Non-dimensional production rate of SGS horizontal temperature flux for the weakly ($\blacktriangle$: $0 < -z/L \leqslant 1$) and strongly convective ($\bigcirc$: $-z/L > 1$) surface layers.

SGS shear stress budget is dominated by the production and pressure destruction terms.

3.4. *SGS temperature flux budgets*

In this section, we discuss the results for the various terms in the budget equations of the SGS horizontal temperature flux, $\langle F_1 \rangle$,

$$0 = \frac{\partial}{\partial x_3} \langle T_{F13}^{(t)} \rangle + \langle P_{F1} \rangle + \langle \mathscr{R}_{F1} \rangle, \tag{3.8}$$

and the SGS vertical temperature flux, $\langle F_3 \rangle$,

$$0 = \frac{\partial}{\partial x_3} \langle T_{F33}^{(t)} \rangle + \langle P_{F3} \rangle + \langle P_{BF3} \rangle + \langle \Pi_{F3} \rangle. \tag{3.9}$$

Again, we assume nominal horizontal homogeneity of the field site, thus the pressure transport term is zero in (3.8). The budget terms are non-dimensionalized by $\kappa z/(T_* u_*^2)$. We summarize the behaviour of the production and pressure terms using fewer curves since their magnitudes vary slowly for $-z/L \gg 1$ as the local free convection condition is approached (Wyngaard *et al.* 1971).

The budget of the SGS horizontal temperature flux, $\langle F_1 \rangle$, given by (3.8), includes the production (due to shear and stratification), the turbulent transport and the pressure–temperature-gradient correlation. The total production rate of $\langle F_1 \rangle$, $\langle P_{F1} \rangle$, is shown in figure 23. For both weakly and strongly convective surface layers, $\langle P_{F1} \rangle$ is positive (a gain) with the largest magnitude at $\Lambda_w/\Delta_f = 0$. It monotonically decreases with increasing Λ_w/Δ_f (decreasing filter width) because the SGS velocity and scalar become less anisotropic (there must be anisotropy for a non-zero heat flux). It also decreases with increasing instability because the turbulence becomes more horizontally isotropic as local free convection is approached. The production rate of $\langle F_1 \rangle$ due to mean shear exceeds production due to stratification (not shown individually), however both terms follow the trends shown in figure 23. Turbulent transport is a gain, but is generally less than 10 % of the production.
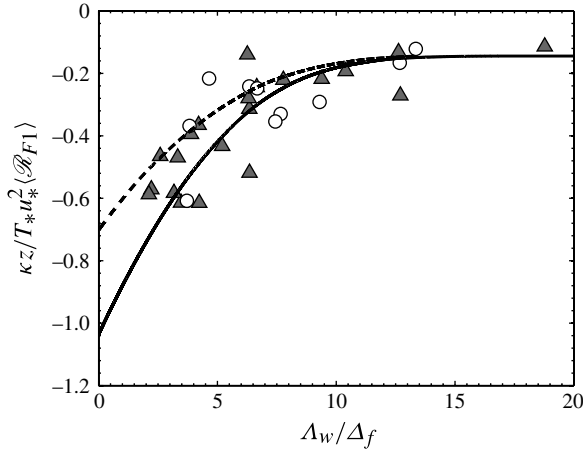
FIGURE 24. Non-dimensional SGS pressure–temperature-gradient correlation in the budget of $\langle F_1 \rangle$ as a function of Λ_w/Δ_f and z/L. The data are grouped as in figure 23.

The pressure–temperature-gradient correlation term in the budget of $\langle F_1 \rangle$, $\langle \mathscr{R}_{F1} \rangle$, is shown in figure 24. For both weakly and strongly convective surface layers, $\langle \mathscr{R}_{F1} \rangle$ is negative, indicating that it is a sink in the budget of $\langle F_1 \rangle$ and acts to drive the turbulence scalar field towards isotropy. It has the maximum magnitude at $\Lambda_w/\Delta_f = 0$, and decreases with increasing Λ_w/Δ_f (decreasing filter width) and increasing instability. The trends and magnitudes of $\langle \mathscr{R}_{F1} \rangle$ agree well with those inferred by Wyngaard *et al.* (1971) (for large filter widths) and approximately balance the measured SGS production (figure 23). The magnitude of the imbalance is within 15 % of the total budget, similar to that obtained by Wilczak & Bedard (2004) for the budget of the total horizontal heat flux.

The budget of the SGS vertical temperature flux, $\langle F_3 \rangle$, given by (3.9), includes the stratification production, the buoyant production, the turbulent transport and the temperature–pressure-gradient correlation (the shear production is zero due to horizontal homogeneity). The SGS stratification production and buoyant production rate of $\langle F_3 \rangle$, $\langle P_{F3} \rangle$ and $\langle P_{BF3} \rangle$, are shown in figures 25 and 26, respectively. For both weakly and strongly convective surface layers, $\langle P_{F3} \rangle$ and $\langle P_{BF3} \rangle$ are negative, indicating production of F_3. The values of the curves for $\Lambda_w/\Delta_f = 0$ are based on the results of Wyngaard *et al.* (1971) for the Reynolds vertical temperature flux, $\langle \theta' u_3' \rangle$. Under unstable conditions, Wyngaard *et al.* (1971) showed that $\langle \theta' u_3' \rangle$ is produced at an essentially constant rate and, hence, the curves for the moderately ($z/L = -0.45$) and strongly ($z/L = -1.70$) convective surface layers should collapse. As the filter width decreases, $\langle P_{F3} \rangle$ should also decrease since the stratification has a diminishing effect on the smaller SGS eddies. Similarly, the rate of buoyant production has the maximum magnitude at $\Lambda_w/\Delta_f = 0$ and increases slowly with $-z/L$ as local free convection is approached. It decreases with the filter width since the effects of buoyancy are diminished.

The temperature–pressure-gradient correlation, $\langle \Pi_{F3} \rangle$, which includes the effects of pressure transport and pressure destruction of $\langle F_3 \rangle$, is positive for both weakly and strongly convective surface layers (figure 27), indicating that it is a sink in the budget of $\langle F_3 \rangle$ and acts to drive the scalar field towards isotropy. It has the maximum magnitude at $\Lambda_w/\Delta_f = 0$ and should increase slowly with $-z/L$ since $\langle P_{F3} \rangle$ and $\langle P_{BF3} \rangle$
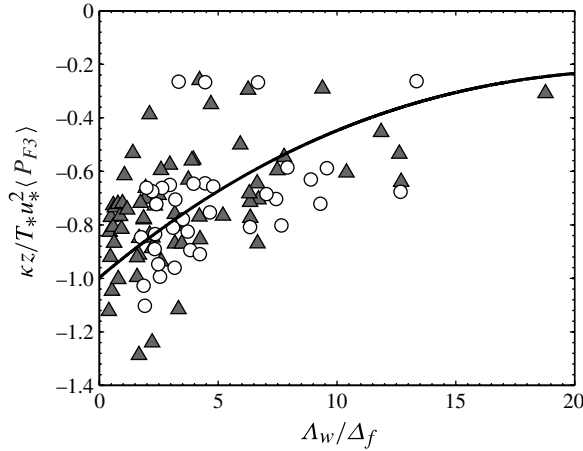
FIGURE 25. Non-dimensional production rate of SGS vertical temperature flux for the weakly (▲: $0 < -z/L \leqslant 1$) and strongly convective (○: $-z/L > 1$) surface layers.
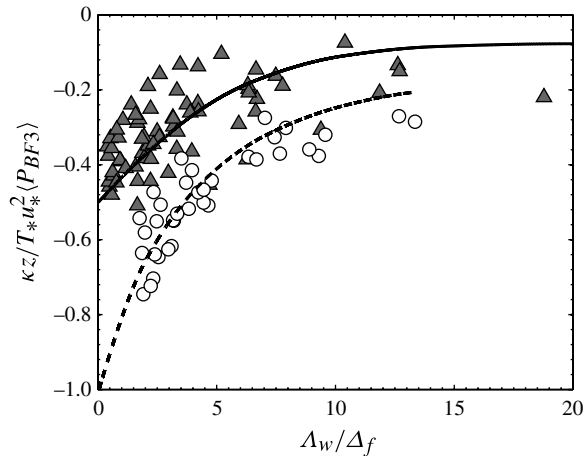

FIGURE 26. Non-dimensional buoyant production rate of SGS vertical temperature flux as a function of Λ_w/Δ_f and z/L. The data are grouped as in figure 25.

do the same. Although the trends of $\langle \Pi_{F3} \rangle$ counter those of $\langle P_{F3} \rangle$ and $\langle P_{BF3} \rangle$, our results show that its magnitude is only 50 % of the total production. This imbalance may be due to the attenuation of the measured fluctuating vertical pressure gradient by the finite difference scheme. Note that this attenuation effect is different from that in evaluating the vertical derivative of a statistic (e.g. the SGS pressure transport term in the SGS TKE budget), which is much less affected by the finite spacing.

4. Discussion and conclusions

Turbulence measurement data from the AHATS field campaign were used to analyse the complete budgets of the SGS TKE, the SGS stress and the SGS temperature flux in the convective atmospheric surface layer. In AHATS, the array technique previously
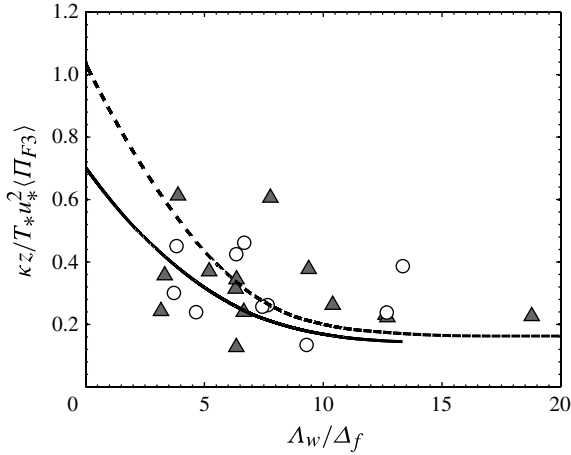
FIGURE 27. Non-dimensional SGS temperature–pressure-gradient correlation in the budget of $\langle F_3 \rangle$ as a function of Λ_w/Δ_f and z/L. The data are grouped as in figure 25.

used to obtain the SGS velocity and temperature was extended to include pressure sensors to measure the fluctuating pressure, enabling separation of the resolvable- and subgrid-scale pressure, and therefore for the first time allowing for all of the terms in the SGS stress and temperature flux transport equations to be obtained.

The results show that for large filter widths the SGS TKE budget is similar to that of the Reynolds stress TKE budget. For near-neutral surface layers, there is a balance between the mechanical production (a gain) and the viscous dissipation (a loss). For unstable surface layers, the gain terms, including the mechanical production, the buoyant production and the SGS pressure transport, are balanced by the loss terms, including the SGS turbulent transport and the viscous dissipation. As the filter width decreases, the buoyancy and transport terms become less significant, and the budget is reduced to a balance between the mechanical production and the viscous dissipation.

Analyses of the SGS stress show that the budgets of the normal components of $\langle \tau_{ij} \rangle$ have more complex behaviours in unstable surface layers than in neutral surface layers due to the interactions among shear, buoyancy, pressure and the presence of the ground. For neutral surface layers and very large filter widths, kinetic energy is supplied to $\langle \tau_{11} \rangle$ through the mean shear (mechanical) production. The pressure–strain-rate correlation transfers a portion of this energy to the $\langle \tau_{22} \rangle$ and $\langle \tau_{33} \rangle$ components. As the filter width decreases, the mechanical production for the latter components become significant. For very small filter widths, there is an eventual approach to equal partitioning of energy among the three normal components and therefore the SGS pressure–strain-rate correlation vanishes.

For unstable surface layers, energy is supplied to $\langle \tau_{11} \rangle$ through the mechanical production and to $\langle \tau_{33} \rangle$ through the buoyant production and the SGS pressure transport. For very large filter widths, the SGS pressure–strain-rate correlation transfers energy from $\langle \tau_{33} \rangle$ to $\langle \tau_{11} \rangle$ and $\langle \tau_{22} \rangle$, while the mechanical production for $\langle \tau_{11} \rangle$ is smaller. Thus, in contrast to neutral surface layers, where the SGS pressure–strain-rate correlation acts to reduce the anisotropy in $\langle \tau_{ij} \rangle$, in unstable surface layers it is the main cause of anisotropy for large filter widths. In this case it contains both the effects of the ground blockage of the vertical downward motions of the large convective eddies and of the tendency to return to isotropy, with the former dominating. For

smaller filter widths, the ground blockage effect is reduced and the effects of return to isotropy become relatively more important, therefore the pressure–strain-rate correlation reverses role and acts to transfer energy from $\langle \tau_{11} \rangle$ and $\langle \tau_{22} \rangle$ to $\langle \tau_{33} \rangle$. For very small filter widths, we expect $\langle \tau_{ij} \rangle$ to become increasingly more isotropic and the SGS pressure–strain-rate correlation to diminish. There is again an equal partitioning of energy among the three normal components, but with larger magnitudes than for the neutral surface layer.

Unlike those of the normal SGS stress components, the budgets of the SGS shear stress component, $\langle \tau_{13} \rangle$, and the SGS temperature flux components, $\langle F_i \rangle$, are qualitatively similar for neutral and unstable surface layers. They are an approximate balance between production and pressure destruction. This aspect of the budgets is striking given the role played by the pressure transport and turbulent transport terms in the SGS dynamics in the unstable surface layer. In the budget of $\langle F_3 \rangle$, the measured pressure term does not completely balance the production terms, probably due to the finite difference scheme used to evaluate the vertical pressure derivative.

There is some imbalance in the measured budgets (10 % for the SGS TKE, $\langle \tau_{11} \rangle$ and $\langle F_1 \rangle$; 20–30 % for $\langle \tau_{22} \rangle$ and $\langle \tau_{33} \rangle$; and 50 % for $\langle F_3 \rangle$). However, the trends of the terms are consistent with each other and, for large filter widths, with those of the Reynolds stress and flux. Thus, these imbalances do not affect the conclusions drawn from the results.

The results of the present study have strong implications for modelling the SGS stress and flux. The approximate balance between production and pressure destruction for the mean SGS shear stress and temperature flux for neutral and unstable surface layers and for all filter widths indicates that the pressure plays the usual role of return-to-isotropy in the dynamics of $\langle \tau_{13} \rangle$ and $\langle F_i \rangle$. For unstable surface layers, however, the pressure–strain-rate correlation is the main cause of anisotropy in the normal SGS stress components for large filter widths (and, hence, for the normal Reynolds stress components). This change in the role of the pressure is due to the surface blockage of the large-scale vertical motions: the pressure fluctuations are largely due to the velocity field and its image field (with respect to the surface). Thus, Rotta's model is inconsistent with the measurement results; it has the opposite sign and cannot account for the ground effects for these filter widths. Therefore, using it alone is likely to underestimate the variances of the horizontal velocity components. Previous studies (e.g. Gibson & Launder 1978) have included an additional term to account for wall effects,

$$\mathcal{R}_{ij}^{(w)} = c_1' \frac{\epsilon}{k} \frac{l}{z\kappa} \left(\langle u_3 u_3 \rangle \delta_{ij} - \frac{3}{2} \langle u_i u_3 \rangle \delta_{j3} - \frac{3}{2} \langle u_j u_3 \rangle \delta_{i3} \right), \qquad (4.1)$$

where $c_1' = 0.5$ and $l = -\langle u_1 u_3 \rangle^{3/2}/\epsilon$ is a length scale, which is approximately proportional to the integral length scale of the vertical velocity. In the surface layer, l/z should be approximately constant and the contribution from $\mathcal{R}_{ij}^{(w)}$ is determined only by $\langle u_i' u_j' \rangle$. Thus, the model effectively assumes that the ground blockage effects come from eddies of scale l, which would be valid for neutral boundary layers. In convective boundary layers, however, the large-scale convective eddies have length and velocity scales (z_i and w_*, respectively) much larger than the surface-layer scales (z and u_*) and ground blockage of these eddies results in much stronger pressure fluctuations than in neutral surface layers. Thus, for Reynolds stress models and transport equation-based SGS models with large filter scales, new models of $\mathcal{R}_{ij}$ reflecting the surface blockage of the large convective eddies are needed.

For very small filter widths, the effects of the surface are weaker and the pressure–strain-rate correlation causes return to isotropy. For intermediate filter widths, there is a competition between return to isotropy and ground blockage effects. Properly modelling these effects is expected to be important for predicting the SGS anisotropy.

Acknowledgements

Supplementary photos

Supplementary photos are available at http://dx.doi.org/10.1017/jfm.2013.302.

REFERENCES

BARDINA, J., FERZIGER, J. H. & REYNOLDS, W. C. 1980 Improved subgrid-scale models for large-eddy simulation. *AIAA Paper* 80-1357.

BORUE, V. & ORSZAG, S. 1998 Local energy flux and subgrid-scale statistics in three-dimensional turbulence. *J. Fluid Mech.* **366**, 1–31.

BOU-ZEID, E., HIGGINS, C., HUWALD, H., MENEVEAU, C. & PARLANGE, M. B. 2010 Field study of the dynamics and modelling of subgrid-scale turbulence in a stable atmospheric surface layer over a glacier. *J. Fluid Mech.* **665**, 480–515.

BRADLEY, E. F., ANTONIA, R. A. & CHAMBERS, A. J. 1981 Turbulence Reynolds number and the turbulent kinetic energy balance in the atmospheric surface layer. *Boundary-Layer Meteorol.* **21**, 183–197.

CAUGHEY, S. J. & WYNGAARD, J. C. 1979 The turbulence kinetic energy budget in convective conditions. *Q. J. R. Meteorol. Soc.* **105**, 231–239.

CERUTTI, S., MENEVEAU, C. & KNIO, O. M. 2000 Spectral and hyper eddy viscosity in high-Reynolds-number turbulence. *J. Fluid Mech.* **421**, 307–338.

CHEN, Q., LIU, S. & TONG, C. 2010 Investigation of the subgrid-scale fluxes and their production rates in a convective atmospheric surface layer using measurement data. *J. Fluid Mech.* **660**, 282–315.

CHEN, Q. & TONG, C. 2006 Investigation of the subgrid-scale stress and its production rate in a convective atmospheric boundary layer using measurement data. *J. Fluid Mech.* **547**, 65–104.

CHEN, Q., ZHANG, H., WANG, D. & TONG, C. 2003 Subgrid-scale stress and its production rate: conditions for the resolvable-scale velocity probability density function. *J. Turbul.* **4**, N27.

CLARK, R. A., FERZIGER, J. H. & REYNOLDS, W. C. 1979 Evaluation of subgrid-scale models using an accurately simulated turbulent flow. *J. Fluid Mech.* **91**, 1–16.

DEARDORFF, J. W. 1970 A numerical study of three-dimensional turbulent channel flow at large Reynolds numbers. *J. Fluid Mech.* **41**, 453–480.

DEARDORFF, J. W. 1972 Numerical investigation of neutral and unstable planetary boundary layers. *J. Atmos. Sci.* **29**, 91–115.

DEARDORFF, J. W. 1973 The use of subgrid transport equations in a three-dimensional model of atmospheric turbulence. *J. Fluids Engng* **95**, 429–438.

DEARDORFF, J. W. 1980 Stratocumulus-capped mixed layers derived from a three-dimensional model. *Boundary-Layer Meteorol.* **18**, 495–527.

DOMARADZKI, J. A., LIU, W. & BRACHET, M. E. 1993 An analysis of subgrid-scale interactions in numerically simulated isotropic turbulence. *Phys. Fluids* A **5**, 1747–1759.

ELLIOTT, J. A. 1972 Microscale pressure fluctuations measured within the lower atmospheric boundary layer. *J. Fluid Mech.* **53**, 351–383.

FU, S., LAUNDER, B. E. & TSELEPIDAKIS, D. P. 1987 Accommodating the effects of high strain rates in modelling the pressure–strain correlation. *Tech. Rep.* Mechanical Engineering Department Report TFD/87/5, UMIST.

GERMANO, M., PIOMELLI, U., MOIN, P. & CABOT, W. H. 1991 A dynamic subgrid-scale eddy viscosity model. *Phys. Fluids* A **3**, 1760–1765.

GIBSON, M. M. & LAUNDER, B. E. 1978 Ground effects on pressure fluctuations in the atmospheric boundary layer. *J. Fluid Mech.* **86**, 491–511.

HATLEE, S. C. & WYNGAARD, J. C. 2007 Improved subfilter-scale models from the HATS field data. *J. Atmos. Sci.* **64**, 1694–1705.

HIGGINS, C. W., FROIDEVAUX, M., SIMEONOV, V., VERCAUTEREN, N., BARRY, C. & PARLANGE, M. B. 2012 The effect of scale on the applicability of Taylor's frozen turbulence hypothesis in the atmospheric boundary layer. *Boundary-Layer Meteorol.* **143**, 379–391.

HIGGINS, C. W., PARLANGE, M. B. & MENEVEAU, C. 2007 The effect of filter dimension on the subgrid-scale stress, heat flux, and tensor alignments in the atmospheric surface layer. *J. Atmos. Ocean. Tech.* **24**, 360–375.

HÖGSTRÖM, U. 1990 Analysis of turbulence structure in the surface layer with a modified similarity formulation for near neutral conditions. *J. Atmos. Sci.* **47**, 1949–1972.

HORST, T. W., KLEISSL, J., LENSCHOW, D. H., MENEVEAU, C., MOENG, C.-H., PARLANGE, M. B., SULLIVAN, P. P. & WEIL, J. C. 2004 HATS: Field observations to obtain spatially-filtered turbulence fields from transverse arrays of sonic anemometers in the atmosperic surface flux layer. *J. Atmos. Sci.* **61**, 1566–1581.

KAIMAL, J. C. & FINNIGAN, J. J. 1994 *Atmospheric Boundary Layer Flows*. Oxford University Press.

KAIMAL, J. C., WYNGAARD, J. C., IZUMI, Y & COTÉ, O. R. 1972 Spectral characteristic of surface-layer turbulence. *Q. J. R. Meteorol. Soc.* **98**, 563–589.

KHANNA, S. & BRASSEUR, J. G. 1998 Three-dimensional buoyancy- and shear-induced local structure of the atmospheric boundary layer. *J. Atmos. Sci.* **55**, 710–743.

KLEISSL, J, MENEVEAU, C. & PARLANGE, M. 2003 On the magnitude and variability of subgrid-scale eddy-diffusion coefficients in the atmospheric surface layer. *J. Atmos. Sci.* **60**, 2372–2388.

KRISTENSEN, L., MANN, J., ONCLEY, S. P. & WYNGAARD, J. C. 1997 How close is close enough when measuring scalar fluxes with displaced sensors? *J. Atmos. Ocean. Tech.* **14**, 814–821.

LAUNDER, B. E., REECE, G. J. & RODI, W. 1975 Progress in the development of a Reynolds-stress turbulence closure. *J. Fluid Mech.* **68** (3), 537–566.

LENSCHOW, D. H., MANN, J. & KRISTENSEN, L. 1993 How long is long enough when measuring fluxes and other turbulence statistics? *Tech. Rep.* NCAR/TN-389 + STR. National Center for Atmospheric Research.

LENSCHOW, D. H. & RAUPACH, M. R. 1991 The attenuation of fluctuations in scalar concentrations through sampling tubes. *J. Geophys. Res.* **96**, 15259–15268.

LEONARD, A. 1974 Energy cascade in large-eddy simulations of turbulent fluid flows. *Adv. in Geophys.* **18**, 237–248.

LILLY, D. K. 1967 The representation of small-scale turbulence in numerical simulation experiments. In *Proceedings IBM Scientific Computing Symposium on Environmental Science* (ed. H. H. Goldstine). pp. 195–210.

LUDWIG, F. L., CHOW, F. K. & STREET, R. L. 2009 Effect of turbulence models and spatial resolution on resolved velocity structure and momentum fluxes in large-eddy simulations of neutral boundary layer flow. *J. Appl. Meteorol. Climatol.* **48**, 1161–1180.

LUMLEY, J. L. 1965 Interpretation of time spectra measured in high-intensity shear flows. *Phys. Fluids* **6**, 1056–1062.

LUMLEY, J. L. 1978 Computational modelling of turbulent flows. *Adv. Appl. Mech.* **18**, 123–176.

LUMLEY, J. L. 1983 Turbulence modelling. *J. Appl. Mech.* **50**, 1097–1103.

MASON, P. J. 1994 Large-eddy simulation: a critical review of the technique. *Q. J. R. Meteorol. Soc.* **120**, 1–26.

MASON, P. J. & BROWN, A. R. 1994 The sensitivity of large-eddy simulations of turbulent shear flow to subgrid models. *Boundary-Layer Meteorol.* **70**, 133–150.

MASON, P. J. & THOMSON, D. J. 1992 Stochastic backscatter in large-eddy simulations of boundary layers. *J. Fluid Mech.* **242**, 51–78.

McBean, G. A. & Elliott, J. A. 1975 The vertical transports of kinetic energy by turbulence and pressure in the boundary layer. *J. Atmos. Sci.* **32**, 753–766.

Meneveau, C., Lund, T. S. & Cabot, W. H. 1996 A Lagrangian dynamic subgrid-scale model of turbulence. *J. Fluid Mech.* **319**, 353–385.

Métais, O. & Lesieur, M. 1992 Spectral large eddy simulation of isotropic and stably stratified turbulence. *J. Fluid Mech.* **239**, 157–194.

Miller, D. O., Tong, C. & Wyngaard, J. C. 1999 The effects of probe-induced flow distortion on velocity covariances: field observations. *Boundary-Layer Meteorol.* **91**, 483–493.

Nieuwstadt, F. T. M., Mason, P. J., Moeng, C.-H. & Schumann, U. 1991 Large-eddy simulation of the convective boundary layer: a comparison of four computer codes. In *Turbulent Shear Flows 8* (ed. F. Durst, R. Friedrich, B. E. Launder, F. W. Schmidt, U. Schumann & J. H. Whitelaw), pp. 343–367. Springer.

Nieuwstadt, F. T. M. & de Valk, P. J. P. M. M. 1987 A large eddy simulation of buoyant and non-buoyant plume dispersion in the atmospheric boundary layer. *Atmos. Environ.* **21**, 2573–2587.

Nishiyama, R. T. & Bedard, A. J. 1991 A quad-disk static pressure probe for measurement in adverse atmospheres – with a comparative review of static pressure probe designs. *Rev. Sci. Instrum.* **62**, 2193–2204.

Patton, E. G., Horst, T. W., Sullivan, P. P., Lenschow, D. H., Oncley, S. P., Brown, W. O. J., Burns, S. P., Guenther, A. B., Held, A., Karl, T., Mayor, S. D., Rizzo, L. V., Spuler, S. M., Sun, J., Turnipseed, A. A., Allwine, E. J., Edburg, S. L., Lamb, B. K., Avissar, R., Calhoun, R. J., Kleissl, J., Massman, W. J., Paw-U, K. T. & Weil, J. C. 2011 The canopy horizontal array turbulence study. *Bull. Amer. Meteorol. Soc.* **92**, 593–611.

Peltier, L. J., Wyngaard, J. C., Khanna, S. & Brasseur, J. 1996 Spectra in the unstable surface layer. *J. Atmos. Sci.* **53**, 49–61.

Pope, S. B. 2000 *Turbulent Flows*. Cambridge University Press.

Porté-Agel, F., Parlange, M. B., Meneveau, C. & Eichinger, W. E. 2001 *A priori* field study of the subgrid-scale heat fluxes and dissipation in the atmospheric surface layer. *J. Atmos. Sci.* **58**, 2673–2698.

Porté-Agel, F., Parlange, M. B., Meneveau, C., Eichinger, W. E. & Pahlow, M. 2000 Subgrid-scale dissipation in the atmospheric surface layer: effects of stability and filter dimension. *J. Atmos. Sci.* **1**, 75–87.

Rajagopalan, A. G. & Tong, C. 2003 Experimental investigation of scalar–scalar-dissipation filtered joint density function and its transport equation. *Phys. Fluids* **15**, 227–244.

Ramachandran, S. & Wyngaard, J. C. 2011 Subfilter-scale modelling using transport equations: large-eddy simulation of the moderately convective atmospheric boundary layer. *Boundary-Layer Meteorol.* **139**, 1–35.

Rotta, J. C. 1951 Statistische theorie nichthomogener turbulenz. *Z. Phys.* **129**, 547–572.

Schumann, U. 1975 Subgrid scale model for finite difference simulations of turbulent flows in plane channels and annuli. *J. Comput. Phys.* **18**, 376–404.

Shih, T.-H. & Lumley, J. L. 1985 Modelling of pressure correlation terms in Reynolds stress and scalar flux equations. *Tech. Rep.* FDA 85-5. Cornell University.

Smagorinsky, J. 1963 General circulation experiments with the primitive equations: I. The basic equations. *Mon. Weath. Rev.* **91**, 99–164.

Sullivan, P. P., Edson, J. B., Horst, T. W., Wyngaard, J. C. & Kelly, M. 2006 Subfilter scale fluxes in the marine surface layer: results from the ocean horizontal array turbulence study (OHATS). In *17th Symposium on Boundary Layers and Turbulence, San Diego, CA*. American Meteorological Society.

Sullivan, P. P., Horst, T. W., Lenschow, D. H., Moeng, C.-H. & Weil, J. C. 2003 Structure of subfilter-scale fluxes in the atmospheric surface layer with application to large-eddy simulation modelling. *J. Fluid Mech.* **482**, 101–139.

Tong, C. 2001 Measurements of conserved scalar filtered density function in a turbulent jet. *Phys. Fluids* **13**, 2923–2937.

Tong, C., Wyngaard, J. C. & Brasseur, J. G. 1999 Experimental study of subgrid-scale stress in the atmospheric surface layer. *J. Atmos. Sci.* **56**, 2277–2292.

TONG, C., WYNGAARD, J. C., KHANNA, S. & BRASSEUR, J. G. 1997 Resolvable- and subgrid-scale measurement in the atmospheric surface layer. In *12th Symposium on Boundary Layers and Turbulence, Vancouver, BC, Canada*, pp. 221–222. American Meteorological Society.

TONG, C., WYNGAARD, J. C., KHANNA, S. & BRASSEUR, J. G. 1998 Resolvable- and subgrid-scale measurement in the atmospheric surface layer: technique and issues. *J. Atmos. Sci.* **55**, 3114–3126.

VREMAN, B., GEURTS, B. & KUERTEN, H. 1994 On the formulation of the dynamic mixed subgrid-scale model. *Phys. Fluids* **6**, 4057–4059.

WANG, D. & TONG, C. 2002 Conditionally filtered scalar dissipation, scalar diffusion, and velocity in a turbulent jet. *Phys. Fluids* **14**, 2170–2185.

WANG, D., TONG, C. & POPE, S. B. 2004 Experimental study of velocity filtered joint density function and its transport equation. *Phys. Fluids* **16**, 3599–3613.

WILCZAK, J. M. & BEDARD, A. J. 2004 A new turbulence microbarometer and its evaluation using the budget of horizontal heat flux. *J. Atmos. Ocean. Tech.* **21**, 1170–1181.

WILCZAK, J. M. & BUSINGER, J. A. 1984 Large-scale eddies in the unstably stratified atmospheric surface layers. Part II: Turbulent pressure fluctuations and the budgets of heat flux, stress and turbulent kinetic energy. *J. Atmos. Sci.* **41**, 3551–3567.

WILCZAK, J. M., ONCLEY, S. P. & STAGE, S. A. 2001 Sonic anemometer tilt correction algorithms. *Boundary-Layer Meteorol.* **99**, 127–150.

WYNGAARD, J. C. 1971 Spatial resolution of a resistance wire temperature sensor. *Phys. Fluids* **14**, 2052–2054.

WYNGAARD, J. C. 1981 The effects of probe-induced flow distortion on atmospheric turbulence measurements. *J. Appl. Meteorol.* **20**, 784–794.

WYNGAARD, J. C. 1992 Atmosperic turbulence. *Annu. Rev. Fluid Mech.* **24**, 205–233.

WYNGAARD, J. C. 2004 Toward numerical modelling in the "terra incognita". *J. Atmos. Sci.* **61**, 1816–1826.

WYNGAARD, J. C. & COTÉ, O. R. 1971 The budgets of turbulent kinetic energy and temperature variance in the atmospheric surface layer. *J. Atmos. Sci.* **28**, 190–201.

WYNGAARD, J. C., COTÉ, O. R. & IZUMI, Y. 1971 Local free convection, similarity, and the budgets of shear stress and heat flux. *J. Atmos. Sci.* **28**, 1171–1182.

WYNGAARD, J. C., SIEGEL, A. & WILCZAK, J. M. 1994 On the response of a turbulent-pressure probe and the measurement of pressure transport. *Boundary-Layer Meteorol.* **69**, 379–396.